C h a p t e r 2

Control over the Graft Polymer Architecture via Ring-Opening Metathesis Polymerization

1. Lin, T.-P.; Chang, A. B.; Chen, H.-Y.; Liberman-Martin, A. L.; Bates, C. M.; Voegtle, M. J.; Bauer, C. A.; Grubbs, R. H. Control of Grafting Density and Distribution in Graft Polymers by Living Ring-Opening Metathesis Copolymerization. *J. Am. Chem. Soc.* **2017**, *139*, 3896–3903.

2. Chang, A. B.;[+] Lin, T.-P.;[+] Thompson, N. B.; Luo, S.-X.; Liberman-Martin, A. L.; Chen, H.-Y.; Grubbs, R. H. Design, Synthesis, and Self-Assembly of Polymers with Tailored Graft Distributions. *J. Am. Chem. Soc.* **2017**, *139*, 17683–17693. ([+]*Equal contributions.*)

ABSTRACT

Grafting density and graft distribution impact the chain dimensions and physical properties of polymers. However, achieving precise control over these structural parameters presents long-standing synthetic challenges. In this chapter, we introduce a versatile strategy to synthesize polymers with tailored architectures via grafting-through ring-opening metathesis polymerization (ROMP). One-pot copolymerization of an ω-norbornenyl macromonomer and a discrete norbornenyl co-monomer (diluent) provides opportunities to control the backbone sequence and therefore the side chain distribution. Toward sequence control, the homopolymerization kinetics of 23 diluents were studied, representing diverse variations in the stereochemistry, anchor groups, and substituents. These modifications tuned the homopolymerization rate constants over two orders of magnitude ($0.36\ M^{-1}\ s^{-1} < k_{homo} < 82\ M^{-1}\ s^{-1}$). Rate trends were identified and elucidated by complementary mechanistic and density functional theory (DFT) studies. Building on this foundation, complex architectures were achieved through copolymerizations of selected diluents with a poly(D,L-lactide) (**PLA**), polydimethylsiloxane (**PDMS**), or polystyrene (**PS**) macromonomer. The cross-propagation rate constants were obtained by non-linear least squares fitting of the instantaneous co-monomer concentrations according to the Mayo-Lewis terminal model. In-depth kinetic analyses indicate a wide range of

accessible macromonomer/diluent reactivity ratios ($0.08 < r_1/r_2 < 20$), corresponding to blocky, gradient, or random backbone sequences. Collectively, the insights provided herein into the ROMP mechanism, monomer design, and homo- and copolymerization rate trends offer a general strategy for the design and synthesis of graft polymers with arbitrary architectures. Controlled copolymerization therefore expands the parameter space for molecular and materials design.

Table of Contents

2-1 Introduction

Molecular architecture impacts the chemical and physical properties of all polymers. Achieving precise control over the chain connectivity, sequence, and symmetry presents synthetic challenges as well as rich opportunities for materials design. Over the past several decades, advances in controlled polymerization have enabled the synthesis of polymers with complex architectures.[1-4] Graft polymers are a class of such nonlinear architectures featuring polymeric side chains attached to a polymeric backbone. The grafting density and distribution of grafts along the backbone determine the steric interactions between side chains and in turn influence the physical properties. Graft polymers display many unique properties compared to their linear analogues, such as extended chain conformations,[5-8] increased entanglement molecular weights,[9-12] and architecture-dependent rheological behavior.[13-16] Recent studies have harnessed these properties in a wide variety of applications in photonics,[17-19] drug delivery,[20-22] transport,[23-

[24] and thermoplastics.[25-26] Continued progress in synthetic command over polymer architecture enables further studies of structure-property relationships and inspires new potential applications.

Graft polymers represent ideal platforms to study how chain connectivity defines nanostructures and thereby physical properties. Despite the importance of grafting density and graft distribution, synthetic strategies that permit precise control of these parameters are currently limited. Grafting-to[27-30] and grafting-from[31-34] approaches require multiple steps in which side chains are either attached to or grown from a pre-formed backbone. Steric congestion along the backbone typically prevents precise control over the molecular weight, grafting density, and side chain distribution. As a result, the synthesis of well-defined *architectural* variants – let alone materials with variable *chemical* compositions – is challenging. Grafting-through ring-opening metathesis polymerization (ROMP) closes this gap by affording wide functional group tolerance and enabling simultaneous control over side chain and backbone lengths.[35-37] In this chapter, we will first introduce a ROMP strategy that provides access to polymers with uniform grafting densities spanning the linear to bottlebrush regimes (Sections 2-2 to 2-7). We will then expand the scope of architectural design to graft polymers with tapered and blocky graft distributions (Sections 2-8 to 2-11).

Our approach employs controlled copolymerization of a macromonomer and a small-molecule diluent. The relative reactivity of the two co-monomers directly dictates the spatial arrangement of the side chains. For example, if the macromonomer and diluent copolymerize at approximately the same rate, the side chains are therefore uniformly distributed along the polymer backbone (Figure 2.1A). Such polymers are widely termed "cylindrical molecular brushes" due to their steric-induced stiffness and axes of symmetry.[38-42] These cylindrical brushes can be modeled as wormlike chains with the same average cross-sectional radius (R_c) along the entire backbone.[5,43-45] On the other hand, if the macromonomer and diluent copolymerize at different rates, the resulting gradient sequences are anticipated to template different side chain conformations. Depending on the extent of side chain stretching, R_c varies and tapered, non-cylindrical molecular shapes result (Figure 2.1B). Control over the co-monomer distribution therefore opens opportunities to manipulate the chain dimensions and physical properties.

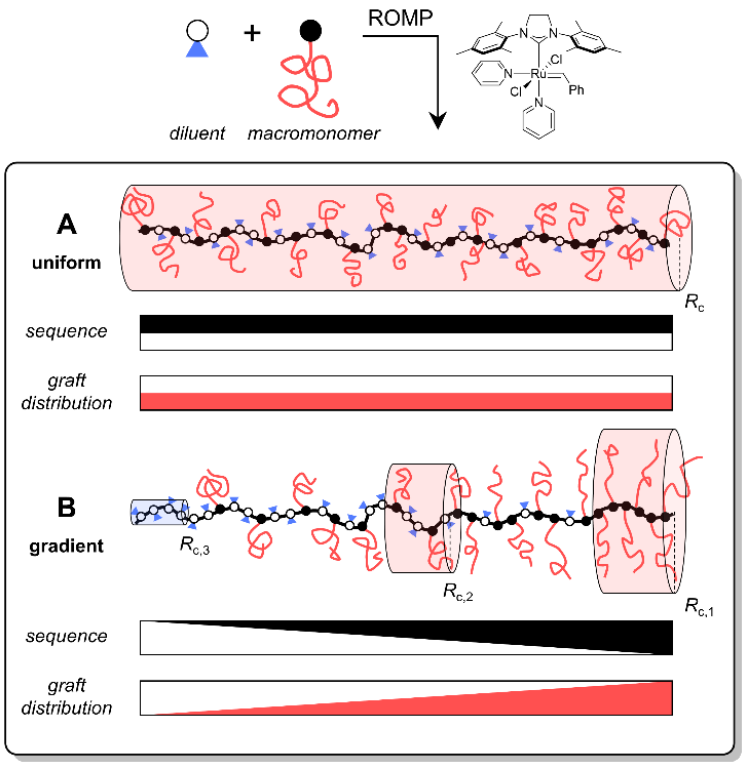

Figure 2.1: Grafting-through ROMP of a small-molecule diluent (*white*) and a macromonomer (*black*). Since the side chains (*red*) are connected to certain backbone units, control over the backbone sequence directly determines the side chain distribution: (*A*) uniform, (*B*) gradient, etc. The anticipated average cross-sectional radius of gyration (R_c) is indicated. For ease of visualization, chains are illustrated in the limit of fully extended backbones.

In this work, we provide the first demonstration that varying the stereochemistry and steric profiles of discrete co-monomers enables the synthesis of well-defined polymers with tunable grafting density and graft distribution. We will first discuss the homopolymerization kinetics of three ω-norbornenyl macromonomers and three discrete norbornenyl diluents, then build complexity through controlled copolymerizations. Trends in the homo- and cross-propagation rates will be outlined to provide guidance for the future rational design of polymer architectures with arbitrary graft chemistry and distribution. In Chapter 3 of this thesis, we will discuss the physical consequences of varying the grafting density and graft distribution in the contexts of block polymer self-assembly and rheology. Living ROMP enables these diverse studies, providing new opportunities for molecular and materials design.

2-2 Monomer Design

In pursuit of control over the graft polymer architecture, the homopolymerization kinetics of macromonomers and diluents were first investigated. Cyclic olefinic monomers that inherently favor alternating sequences were avoided,[46-47] since strict alternation would only afford 50% grafting density and preclude control over the graft distribution. Norbornene-functionalized derivatives, which rarely result in alternating polynorbornenes,[48-50] were selected for the present study. Relief of the high ring strain in norbornene, mediated by highly active ruthenium metathesis catalysts, enables grafting-through ROMP to produce well-defined bottlebrush polymers.[51-53] We note that random copolymerizations of norbornenes have been previously inferred,[52,54-55] suggesting potential opportunities for advanced sequence control; however, quantitative sequence determinations are lacking. For the present studies, ω-norbornenyl polystyrene (**PS**, M_n = 3990 g/mol), polylactide (**PLA**, M_n = 3230 g/mol), and polydimethylsiloxane (**PDMS**, M_n = 1280 g/mol) macromonomers featuring an *exo*-imide anchor group were prepared (Figure 2.2). (Synthetic details are provided in Appendix A, Section A-2.) **PS** and **PLA** macromonomers of similar molecular weights have been previously employed in the synthesis of well-defined bottlebrush polymers,[19,23] making them attractive candidates for our studies. For the small-molecule diluents, we explored a family of *endo*,*exo*-norbornenyl diesters (dimethyl **DME**, diethyl **DEE**, di-*n*-butyl **DBE**, each with molecular weight <300 g/mol) that could be easily assembled by Diels-Alder reactions of cyclopentadiene and the appropriate fumarate (Appendix A, Section A-3). We anticipated different propagation rates for these norbornenyl diesters,[56] amenable to tuning the relative reactivity of diverse diluent/macromonomer pairs. Section 2.8 of this chapter expands the scope of monomer design to other types of diluents.

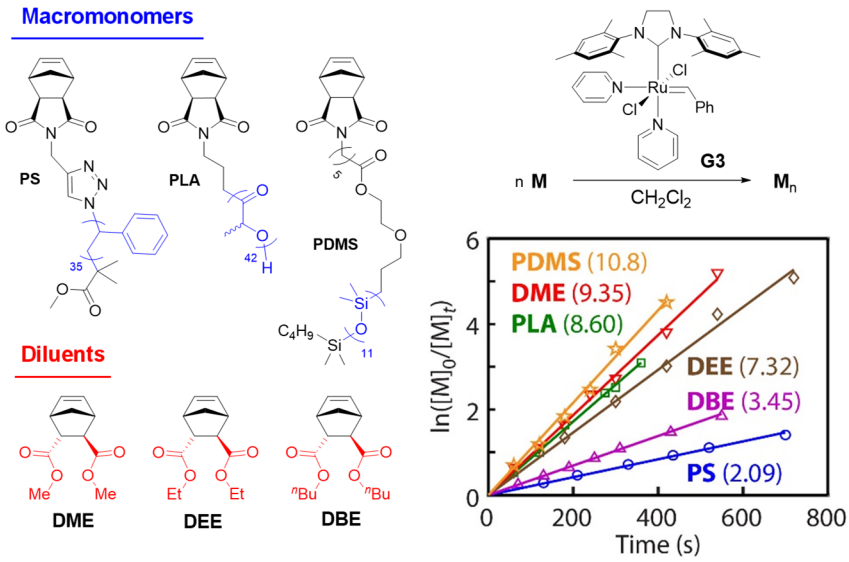

Figure 2.2: (*left*) Structures of macromonomers (**PS**, **PLA**, **PDMS**) and diluents (**DME**, **DEE**, **DBE**). (*right*) Plots of $\ln([M]_0/[M]_t)$ versus time, showing first-order kinetics for the homopolymerization of norbornene monomers (0.05 M) catalyzed by **G3** (0.5 mM) in CH_2Cl_2 at 298 K (orange stars: **PDMS**, inverted red triangles: **DME**, green squares: **PLA**, brown diamonds: **DEE**, purple triangles: **DBE**, blue circles = **PS**). The numbers in parentheses indicate k_{obs} (10^{-3} s^{-1}) under the reaction conditions.

2-3 Homopolymerization Kinetics

ROMP of each monomer in CH_2Cl_2 (0.05 M) was mediated by the highly active third-generation olefin metathesis catalyst,[57] $(H_2IMes)(pyr)_2(Cl)_2Ru{=}CHPh$ (**G3**, 0.5 mM). At different time points, aliquots were extracted from the reaction mixture and immediately quenched in a separate vial containing a large excess of ethyl vinyl ether. Subsequently, the quenched reactions were analyzed by size-exclusion chromatography (SEC) and ^{1}H NMR spectroscopy, allowing evaluation of the conversion, molecular weight, and molecular weight dispersity. (See Appendix A, Section A-4 for standard procedures.) As shown in Figure 2.2, the depletion of monomers is first-order. Since the rate of initiation for **G3** is much faster than that of propagation under these conditions,[57-58] the observed first-order rate constant (k_{obs}) can be used to calculate the second-order self-propagation rate constant (k_{homo}) according to Eq. 2-1 (M = monomer):

$$-\frac{d[M]_t}{dt} = k_{obs}[M]_t = k_{homo}[G3]_0[M]_t \qquad \text{Eq. 2-1}$$

For many monomers, the rate constants were determined at least in triplicate. The calculated values typically varied by no more than five percent (Figure 2.3).

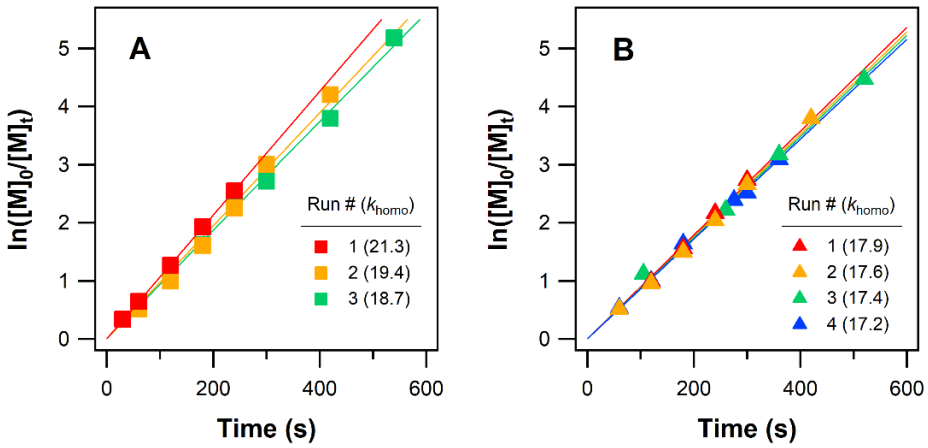

Figure 2.3: Representative repeated runs to determine k_{homo} (M^{-1} s^{-1}) for (*A*) **DME** and (*B*) and **PLA**. For all diluents and macromonomers studied herein, the measured rate constants are consistent across multiple runs.

The rate constant k_{homo}, which is independent of the catalyst concentration, is directly relevant to our copolymerization kinetic analyses. The homopolymerization kinetic results are summarized in Table 2.1.

Table 2.1: Homopolymerizations of macromonomers and diluents in CH_2Cl_2 at 298 K.

Monomer	k_{homo} (M^{-1} s^{-1})	Expected M_n[a] (kg/mol)	Measured M_n[b] (kg/mol)	$Đ$[b]	Conv. (%)
PS	4.18	399	375	1.06	94[c]
PLA	17.2	323	319	1.01	99[c]
PDMS	21.6	128	131	1.02	99[c]
DME	18.7	21.0	21.7	1.02	100[d]
DEE	14.6	23.8	24.2	1.02	100[d]
DBE	6.90	29.4	29.6	1.02	100[d]

[a] Based on [M]:[**G3**] = 100:1.
[b] Determined by SEC light scattering detector.
[c] Determined by SEC differential refractive index detector.
[d] Determined by ^{1}H NMR.

Comparing the three macromonomers, **PDMS** possesses the largest k_{homo} (21.6 M^{-1} s^{-1}). The k_{homo} of **PLA** (17.2 M^{-1} s^{-1}) is around four times as large as that measured for **PS** (4.18 M^{-1} s^{-1}), consistent with previous observations.[52] The k_{homo} values of the norbornenyl diesters trend inversely with the bulkiness of the ester substituents as anticipated. Indeed,

the k_{homo} measured for **DME** (18.7 M^{-1} s^{-1}) is larger than that of **DEE** (14.6 M^{-1} s^{-1}) or **DBE** (6.90 M^{-1} s^{-1}). Collectively, these results reinforce the important role that the norbornene monomer sterics play in the rate of ROMP. Sections 2-8 and 2-9 will expand the scope of monomer design and further explore the role of steric effects.

2-4 Developing an Analytical Method for Copolymerization Kinetics

Homopolymerization kinetic analyses indicate that ROMP of each individual macromonomer or diluent is well-behaved. However, controlling side chain density and distribution also requires studying the *copolymerization* kinetics. The copolymerization kinetics were analyzed based on the Mayo-Lewis terminal model.[59-60] The terminal model assumes that, for a mixture of two monomers M_1 and M_2, there are two propagating species (M_1* and M_2*) whose reactivities solely depend on the last-incorporated monomer.[59] The copolymerization kinetics can be captured by four propagation reactions involving M_1* and M_2*, each described by a unique rate constant k. Scheme 2.1 shows the relevant reactions for a mixture of a discrete diluent (M_2) and a macromonomer (M_1): (A) diluent self-propagation (M_2* → M_2*, k_{22}), (B) cross-propagation via addition of M_1 to M_2* (M_2* → M_1*, k_{21}), (C) macromonomer self-propagation (M_1* → M_1*, k_{11}), and (D) cross-propagation via addition of M_2 to M_1* (M_1* → M_2*, k_{12}).

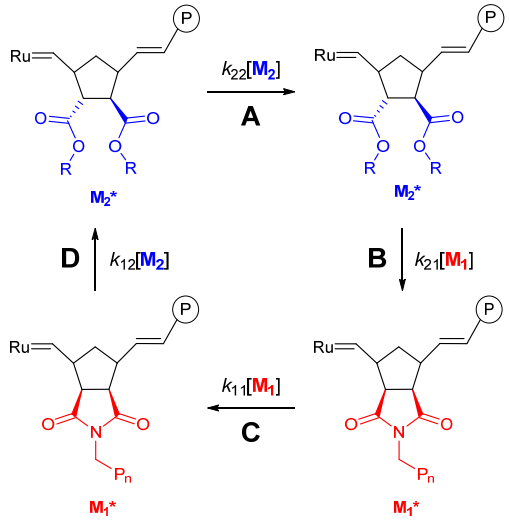

Scheme 2.1: Propagation reactions for the copolymerization of a discrete diluent (M_2, *dx*-DE shown for example) and a macromonomer (M_1) according to a terminal model. M_2* and M_1* are the corresponding propagating alkylidene species. (*A*) Diluent self-propagation (k_{22}), (*B*) cross-propagation (k_{21}), (*C*) macromonomer self-propagation (k_{11}), (*D*) cross-propagation (k_{12}).

The reactivity ratios ($r_1 = k_{11}/k_{12}$, $r_2 = k_{22}/k_{21}$) are defined by the tendency for the propagating species to react with the same monomer over the other. As depicted in Scheme 2.2, the copolymerization is inherently directed by the reactivity ratios, leading to sequences such as alternating, blocky, random, or gradient.

Over the past several decades, a number of methods have been established to determine the reactivity ratios for copolymerizations. Popular techniques include the Mayo-Lewis,[59-60] Fineman-Ross,[61] and Kelen-Tüdös[62] methods, among others.[63] The validity of these linear regression methods has been established in many contexts; however, we note that they are derived from equations based on the steady-state approximation, with the assumption that the rates of crossover are identical: that is, $k_{12}[M_1^*]_t[M_2]_t = k_{21}[M_2^*]_t[M_1]_t$. As such, these methods are only strictly valid under steady-state conditions in which the change in monomer feed is insignificant.[64] Obtaining kinetic data in the required low-conversion regime is prohibitively challenging for fast polymerization reactions such as **G3**-mediated ROMP. Due to this constraint, a new analytical approach that bypasses the steady-state approximation is needed.

Scheme 2.2: Mayo-Lewis terminal model describing the copolymerization of M_1 and M_2.

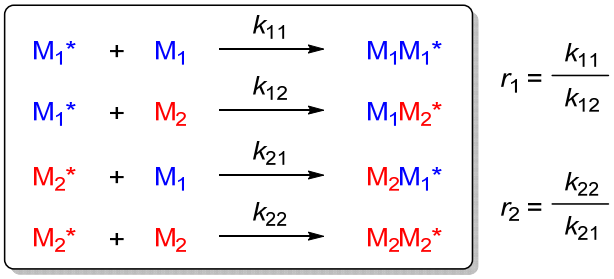

Case I: $r_1, r_2 << 1$ (alternating)

$M_1M_2M_1M_2M_1M_2M_1M_2M_1M_2M_1M_2M_1M_2M_1M_2M_1M_2M_1M_2$

Case II: $r_1, r_2 >> 1$ (blocky)

$M_1M_1M_1M_1M_1M_1M_1M_1M_1M_1M_1M_2M_2M_2M_2M_2M_2M_2M_2M_2M_2$

Case III: $r_1 = r_2 = 1$ (random)

$M_2M_2M_1M_2M_1M_1M_1M_2M_1M_2M_1M_2M_2M_1M_1M_2M_1M_2M_2M_1$

Case IV: $r_1 < 1 < r_2$ (gradient)

$M_2M_2M_2M_2M_1M_2M_2M_2M_1M_1M_2M_2M_1M_1M_1M_2M_1M_1M_1M_1$

According to the terminal model, the time-dependent concentrations of M_1, M_2, M_1*, and M_2* can be described by the following differential equations:

$$-\frac{d[M_1]_t}{dt} = k_{11}[M_1^*]_t[M_1]_t + k_{21}[M_2^*]_t[M_1]_t \quad \text{Eq. 2-2}$$

$$-\frac{d[M_2]_t}{dt} = k_{12}[M_1^*]_t[M_2]_t + k_{22}[M_2^*]_t[M_2]_t \quad \text{Eq. 2-3}$$

$$-\frac{d[M_1^*]_t}{dt} = k_{12}[M_1^*]_t[M_2]_t - k_{21}[M_2^*]_t[M_1]_t \quad \text{Eq. 2-4}$$

$$-\frac{d[M_2^*]_t}{dt} = k_{21}[M_2^*]_t[M_1]_t - k_{12}[M_1^*]_t[M_2]_t \quad \text{Eq. 2-5}$$

While exact analytical solutions for Eqs. 2-2 to 2-5 cannot be obtained, numerical solutions for $[M_1]_t$, $[M_2]_t$, $[M_1^*]_t$, and $[M_2^*]_t$ can be found if the propagation rate constants are known. In our study, the homopolymerization rate constants k_{11} and k_{22} can be independently measured (Table 2.1). Furthermore, the instantaneous monomer concentrations $[M_1]_t$ and $[M_2]_t$ during the copolymerization can be determined by quenching aliquots at known times t, and in living ROMP, the sum of $[M_1^*]_t$ and $[M_2^*]_t$ should be $[\mathbf{G3}]_0$. As a result, the best numerical solutions for k_{12} and k_{21} can be determined using a non-linear least-square curve fitting method.

2-5 Copolymerization Kinetics

We first investigated the copolymerization of **PS** (0.05 M) and **DME** (0.05 M) mediated by **G3** (0.5 mM) in CH_2Cl_2 (Figure 2.4A). The conditions, including the monomer and catalyst concentrations, were identical to those employed in homopolymerization reactions. Aliquots were extracted at different time points, quenched, and subjected to SEC and NMR analyses. The SEC traces indicated the continuing depletion of **PS** as well as the concomitant growth of the copolymer (Figure 2.4B). In addition, the instantaneous concentrations of both monomers could be determined by ^{1}H NMR integration of their distinct norbornenyl olefinic resonances. Plotting $\ln([M]_0/[M]_t)$ as a function of time (Figure 2.4C) suggested that the decay of **PS** and **DME** approached *pseudo* first order. However, we note that first-order kinetics are only strictly applicable in the event that both $[M_1^*]_t$ and $[M_2^*]_t$ are constant (see Eqs. 2-2 and 2-3). With the same

G3 concentration of 0.5 mM, the propagation rates for **PS** and **DME** in the copolymerization reaction were, respectively, faster and slower than those measured independently in the homopolymerization reactions (Figure 2.4C). The increase in the rates of **PS** consumption in the copolymerization reaction could be attributed to cross-propagation being faster than self-propagation. Interestingly, the opposite trend was observed for **DME**.

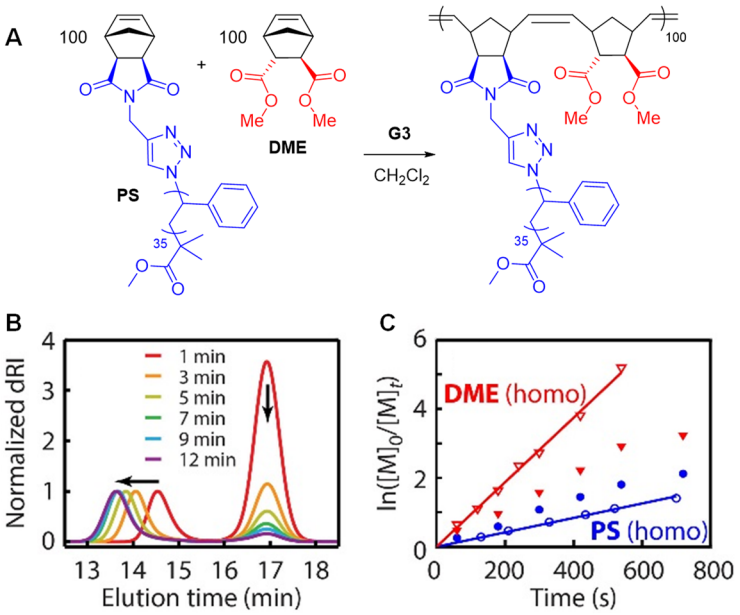

Figure 2.4: (*A*) Copolymerization of **PS** (0.05 M) and **DME** (0.05 M) catalyzed by **G3** (0.5 mM) in CH_2Cl_2 at 298 K. (*B*) Normalized differential refractive index (dRI) trace from size-exclusion chromatography. (*C*) Plots of $\ln([M]_0/[M]_t)$ versus time as monitored by ^{1}H NMR spectroscopy (filled blue circles = **PS**, filled red triangles = **DME**). Unfilled blue circles (**PS**), unfilled red triangles (**DME**), and the solid lines, plotted for comparison, were obtained from homopolymerization reactions under the same conditions.

To gain further insight, the kinetic profile of the copolymerization of **PS** and **DME** (1:1) was fitted to the terminal model using our analytical methods with known values of $k_{PS\text{-}PS}$, $k_{DME\text{-}DME}$, $[\mathbf{PS}]_0$, $[\mathbf{DME}]_0$, and $[\mathbf{G3}]_0$ (Figure 2.5A). The calculated curves of monomer conversion versus total conversion agreed satisfactorily with the experimental data (Figure 2.5B). The calculated rate constants and reactivity ratios for various macromonomer/diluent copolymerization pairs are provided in Table 2.1.

Table 2.1: Copolymerization rate constants and reactivity ratios in CH_2Cl_2 at 298 K.

Entry	M_1	M_2	$[M_1]_0$ (M)	$[M_2]_0$ (M)	k_{11} (M^{-1} s^{-1})	k_{12}[a] (M^{-1} s^{-1})	k_{22} (M^{-1} s^{-1})	k_{21}[a] (M^{-1} s^{-1})	r_1	r_2	r_1r_2
1	PS	DME	0.050	0.050	4.18	7.74	18.7	13.2	0.54	1.41	0.76
2	PS	DME	0.050	0.100	4.18	7.58	18.7	14.6	0.55	1.28	0.71
3	PS	DEE	0.050	0.050	4.18	7.73	14.6	8.75	0.54	1.67	0.90
4	PS	DBE	0.050	0.050	4.18	5.23	6.90	5.66	0.80	1.22	0.97
5	PS	DBE	0.075	0.025	4.18	5.24	6.90	5.93	0.80	1.16	0.93
6	PLA	DME	0.050	0.050	17.2	18.8	18.7	16.9	0.92	1.11	1.02
7	PLA	DBE	0.050	0.050	17.2	16.7	6.90	7.95	1.03	0.87	0.90
8	PDMS	DME	0.050	0.050	21.6	19.9	18.7	19.9	1.09	0.94	1.02
9	PDMS	DBE	0.050	0.055	21.6	19.5	6.90	15.9	1.11	0.43	0.48

[a] Obtained from least-square curve fitting.

Least-squares fitting of the copolymerization data for **PS** and **DME** (1:1) generates $k_{PS\text{-}DME}$ and $k_{DME\text{-}PS}$ values of 7.74 and 13.2 M^{-1} s^{-1}, respectively (Table 2.2, Entry 1). The reactivity ratios (r_{PS} = 0.54, r_{DME} = 1.41) indicate gradient copolymerization and can be used to simulate the instantaneous copolymer composition (Section 2-6). Copolymerizing **PS** and **DME** in a 1:1 feed ratio could therefore be expected to yield a polymer bearing 50% grafting density and a gradient distribution of **PS** side chains. In order to further examine the validity of our methods, the copolymerization of **PS** and **DME** in a 1:2 feed ratio was carried out and subjected to the same analyses (Figure 2.5C–D), yielding comparable $k_{PS\text{-}DME}$ and $k_{DME\text{-}PS}$ values (Table 2.2, Entry 2). As such, these experiments support the ability of the terminal model to capture the copolymerization kinetics of **G3**-catalyzed ROMP.

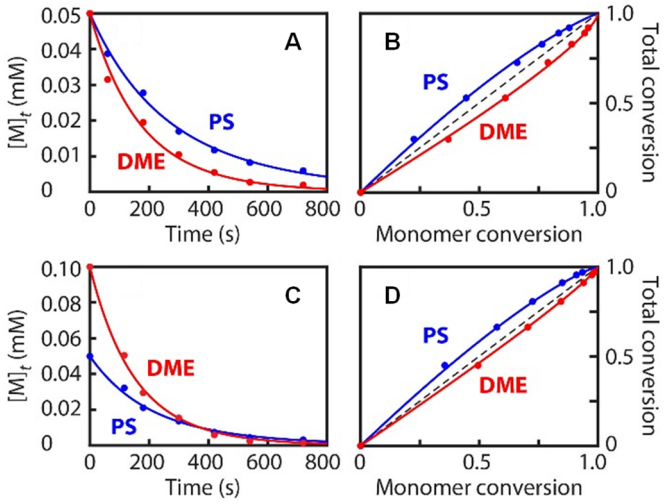

Figure 2.5: Non-linear least-square curve fitting for the copolymerization of (*A*, *B*) **PS** (0.05 M) and **DME** (0.05 M) and (*C*, *D*) **PS** (0.05 M) and **DME** (0.10 M) in CH_2Cl_2 at 298 K. $[\mathbf{G3}]_0$ = 0.5 mM. Calculated fits (solid lines) show close agreement with the measured values (points). In (*B*, *D*), the dashed lines, included for comparison, indicate ideal random copolymerization ($r_1 = r_2 = 1$).

We next examined the 1:1 copolymerization of **PS** and **DEE** (Figure 2.6A–B). The measured $k_{PS\text{-}DEE}$ (7.73 M^{-1} s^{-1}, Table 2.2, Entry 3) is very close to $k_{PS\text{-}DME}$ (7.58–7.74 M^{-1} s^{-1}), indicating similar chemical reactivity of the propagating species **PS*** toward **DME** and **DEE**. In sharp contrast, $k_{DEE\text{-}PS}$ (8.75 M^{-1} s^{-1}) is notably smaller than $k_{DME\text{-}PS}$ (13.2–14.6 M^{-1} s^{-1}). This observation suggests that the **PS*** alkylidene steric/electronic effects

are important in governing the rate of ROMP (perhaps more so than that of the approaching norbornenyl diester). The calculated reactivity ratios r_{PS} (0.54) and r_{DEE} (1.67) indicate gradient copolymerization. In addition, the $r_{PS} \times r_{DEE}$ product of 0.90 suggests an almost ideal copolymerization process in which each propagating species, **PS*** and **DEE***, has the same preference for **PS** over **DEE**; that is, $k_{PS\text{-}PS}/k_{PS\text{-}DME} \approx k_{DME\text{-}PS}/k_{DME\text{-}DME}$. The copolymerizations of **PS** and **DBE** in 1:1 (Figure 2.6C–D) and 3:1 (Figure 2.6E–F) feed ratios have also been examined. The propagation rate constants obtained from these experiments are approximately equal (Table 2.2, Entries 4–5), as expected, again reflecting the competence of our analytical methods. The **PS**/**DBE** copolymerization is best described as near-ideal, approaching random, as evidenced by the reactivity ratios (r_{PS} = 0.8, r_{DBE} = 1.16–1.22) as well as their product ($r_{PS} \times r_{DBE}$ = 0.93–0.97).

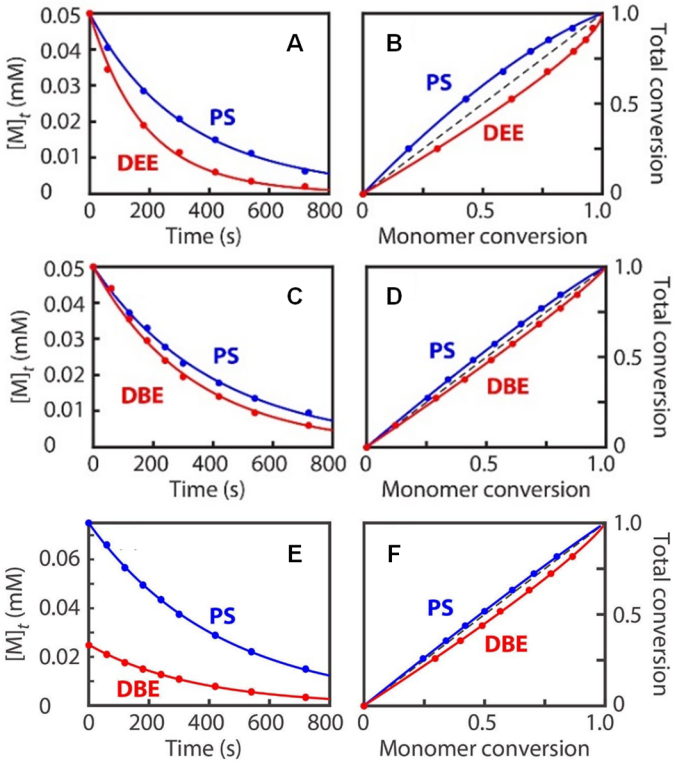

Figure 2.6: Non-linear least-square curve fitting for the copolymerization of various macromonomer/diluent pairs: (*A*, *B*) **PS** (0.05 M) and **DEE** (0.05 M); (*C*, *D*) **PS** (0.05 M) and **DBE** (0.05 M); (*E*, *F*) **PS** (0.075 M) and **DBE** (0.025 M). $[\mathbf{G3}]_0$ = 0.5 mM, solvent = CH_2Cl_2, temperature = 298 K.

For studies and applications in which uniform grafting density is desired, the ability to access random copolymers is crucial. The copolymerization reactions of **PS** with diluents imply that random copolymerization ($r_1 \approx r_2 \approx 1$) might be achieved when both self-propagation rate constants are similar ($k_{11} \approx k_{22}$). To examine this hypothesis, we turned our attention to the copolymerization of **PLA** (k_{homo} = 17.2 M^{-1} s^{-1}) and **DME** (k_{homo} = 18.7 M^{-1} s^{-1}). These experiments indicate that the rate of consumption of **PLA** is only marginally slower than that of **DME**, consistent with an approximately random copolymerization (Figure 2.7A–B; Table 2.2, Entry 6). Similarly, random copolymerization was observed for **PLA**/**DBE** (Figure 2.7C–D; Table 2.2, Entry 7) as well as **PDMS**/**DME** (Figure 2.7E–F; Table 2.2, Entry 8). Lastly, gradient copolymers (Table 2.2, Entry 9; r_{PDMS} = 1.11, r_{DBE} = 0.43) were obtained by copolymerizing **PDMS** with **DBE** (Figure 2.7G–H). The reactivity ratio product ($r_{PDMS} \times r_{DBE}$ = 0.48) indicates a departure from ideal copolymerization. This observation is seemingly correlated with the large differences in the self-propagation rate constants. Taken collectively, the copolymerization of a norbornene-functionalized macromonomer (**PS**, **PLA**, or **PDMS**) with a diluent (**DME**, **DEE**, or **DBE**) could generate either gradient or random copolymers. Kinetic analyses reveal similar k_{12} values (**PS** = 5.23 - 7.74 M^{-1} s^{-1}, **PLA** = 16.7–18.8 M^{-1} s^{-1}, **PDMS** = 19.5–19.9 M^{-1} s^{-1}) and disparate k_{21} values (**PS** = 5.66–14.6 M^{-1} s^{-1}, **PLA** = 7.95–16.9 M^{-1} s^{-1}, **PDMS** = 15.9–19.9 M^{-1} s^{-1}), reflecting the significance of the alkylidene ligands in directing the metathesis rates. This observation could potentially be attributed to the different steric, electronic, and ligating environments exerted by the anchor group (*exo*-imide for macromonomer versus *endo*,*exo*-diester for diluent). The importance of the anchor group has been recently discussed by Matson and coworkers in the context of self-propagation rates.[65] Sections 2-8 and 2-9 in this thesis will further expand the understanding of anchor group effects on ROMP kinetics.

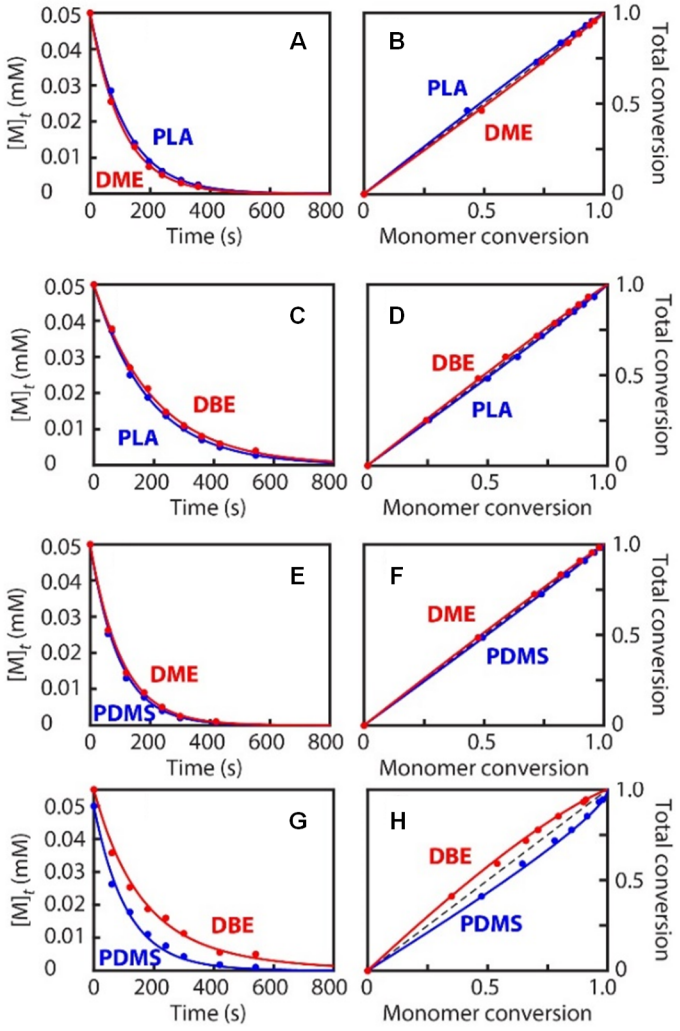

Figure 2.7: Non-linear least-square curve fitting for the copolymerization of various macromonomer/diluent pairs: (*A*, *B*) **PLA**/**DME**; (*C*, *D*) **PLA**/**DBE**; (*E*, *F*) **PDMS**/**DME**; (*G*, *H*) **PDMS**/**DBE** (0.055 M). Reaction conditions: $[M]_0$ = 0.05 M unless otherwise indicated, $[\mathbf{G3}]_0$ = 0.5 mM, solvent = CH_2Cl_2, temperature = 298 K.

2-6 Instantaneous Copolymer Composition

From the copolymerization kinetics, the rate of monomer incorporation at any given time could be calculated according to Eqs. 2-2 and 2-3, allowing the prediction of instantaneous copolymer composition as a function of total conversion. For example, copolymerizing **PS** and **DME** in a 1:1 feed ratio results in (**PS**-*grad*-**DME**)$_n$ best described as a gradient graft polymer (Figure 2.8A). Such a copolymer at 100% conversion possesses, on average, 50% grafting density (*i.e.*, one polystyrene brush per two norbornene backbone repeat units). The difference in reactivity ratios leads to richer **DME** composition at early

conversion and higher **PS** incorporation toward the end. Similar gradient graft polymers have been previously accessed by grafting-from ATRP methods.[33-34] The brush distribution gradient is much less pronounced in copolymers (**PLA**-*ran*-**DME**)$_n$ (Figure 2.8B) and (**PDMS**-*ran*-**DME**)$_n$ (Figure 2.8C), in which the side chains are uniformly grafted across the entire polynorbornene backbone. Lastly, copolymerizing **PDMS**/**DBE** in a 1:1 ratio generates the gradient copolymer (**PDMS**-*grad*-**DBE**)$_n$ (Figure 2.8D). Unlike (**PS**-*grad*-**DME**)$_n$, our simulations indicate that (**PDMS**-*grad*-**DBE**)$_n$ is more densely grafted at early conversion. Coupled with sequential polymerization, copolymerizing **PS**/**DME** and **PDMS**/**DBE** could be exploited in the synthesis of normal tapered or inverse tapered block copolymers.[66] The synthesis of such block copolymers and the impact of molecular architecture on the phase behavior are discussed in Chapter 3.

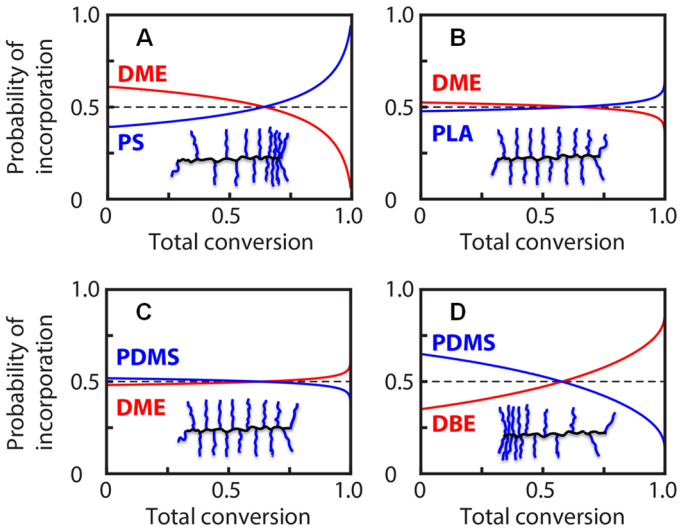

Figure 2.8: Simulated copolymer compositions for (*A*) **PS**:**DME** = 1:1, (*B*) **PLA**:**DME** = 1:1, (*C*) **PDMS**:**DME** = 1:1, and (*D*) **PDMS**:**DBE** = 1:1. Insets show schematic illustrations of the corresponding graft polymers; for ease of visualization, the side chains and backbones are shown in the fully extended limit.

2-7 Synthesis of Architectures with Variable Grafting Density

To showcase the synthetic versatility of our approach, we targeted an array of polymers (**PLA**^{z}-*ran*-**DME**$^{1-z}$)$_n$ with variable grafting densities (z = 1.00, 0.75, 0.50, 0.25) and backbone lengths (n = 167, 133, 100, 67, 33). These polymers could be easily prepared

by mixing **PLA**, **DME**, and **G3** in different ratios according to Eqs. 2-6 and 2-7 (M_1 = macromonomer, M_2 = diluent):

$$z = [M_1]_0 / ([M_1]_0 + [M_2]_0) \quad \text{Eq. 2-6}$$

$$n = ([M_1]_0 + [M_2]_0) / [\mathbf{G3}]_0 \quad \text{Eq. 2-7}$$

These copolymerization reactions were carried out under very mild conditions in CH_2Cl_2 (298 K, $[\mathbf{G3}]_0$ = 0.5 mM, 15 min), and complete monomer consumption was verified by ^{1}H NMR spectroscopy. As shown in Figure 2.9, the SEC analyses of the resulting polymers indicated low dispersities ($Đ$ = 1.01–1.03) as well as excellent agreement between the measured and targeted molecular weights throughout the series (Appendix A, Table A.1).

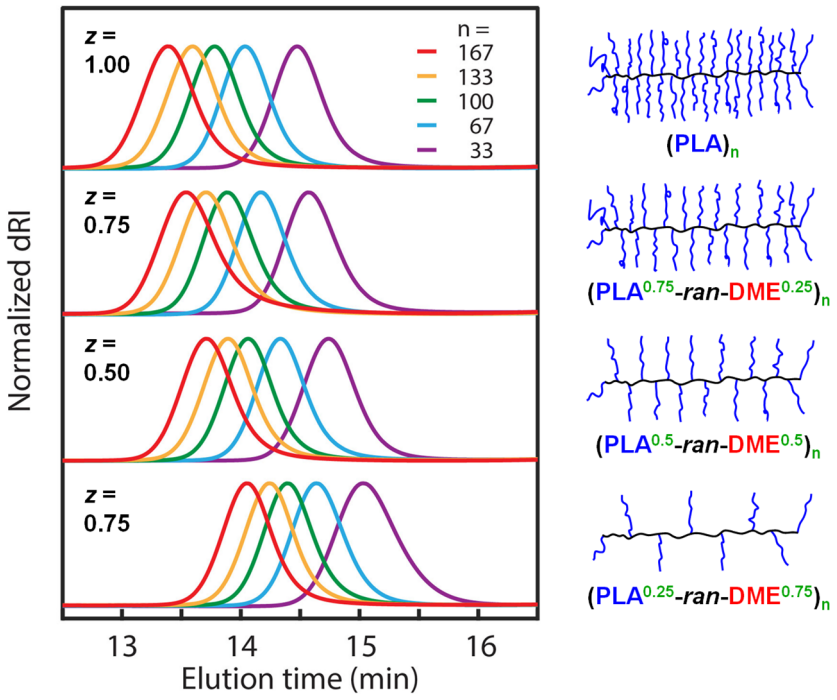

Figure 2.9: SEC traces of (**PLA**^{z}-*ran*-**DME**$^{1-z}$)$_n$ where z = grafting density (1.0, 0.75, 0.50, or 0.25) and n = total backbone degree of polymerization (red: 167, orange: 133, green: 100, blue: 67, purple: 33).

Reinforcing the NMR and SEC data, differential scanning calorimetry (DSC) provided further evidence supporting the incorporation of both macromonomer and diluent (Appendix A, Figure A.5). For example, DSC data collected on (**PS**$^{0.5}$-*ran*-**DBE**$^{0.5}$)$_{200}$ shows glass transition temperature (T_g) at 95 °C, which lies between the T_g values of **PS**$_{100}$ (102 °C) and **DBE**$_{100}$ (71 °C).

2-8 Expanding Monomer Design

Section 2-2 introduced *endo,exo*-norbornenyl dialkylesters as appropriate discrete monomers (diluents) to control the grafting density of polymers with poly(D,L-lactide) (**PLA**, M_n = 3230 g/mol), polydimethylsiloxane (**PDMS**, M_n = 1280 g/mol), or polystyrene (**PS**, M_n = 3990 g/mol) side chains.[67] Across all macromonomer/diluent combinations and feed ratios, kinetic analyses indicated approximately equal rates of co-monomer consumption and therefore approximately uniform side chain distributions. (See for example (**PLA**^{z}-*ran*-**DME**$^{1-z}$)$_n$ in Section 2-7.) Obtaining *non-uniform* side chain distributions requires changing the relative reactivity of the macromonomer and diluent (Figure 2.1B). We propose that designing new small-molecule co-monomers is the most convenient route. This strategy avoids potentially tedious end-group modifications to the macromonomers and retains the synthetic utility of one-pot batch copolymerization. While semi-batch methods (involving continuous addition of one monomer to another) can afford wide control over polymer sequences,[68-69] they require additional instrumentation and optimization of factors such as feed ratio and feed rate.[70-71] Similarly, while sequential addition of macromonomers with different molecular weights can also provide access to tapered architectures,[72] this approach requires the preparation of multiple well-defined macromonomers and fixes the grafting density at 100%.

Scheme 2.3: Expanding monomer design for ring-opening metathesis copolymerization.

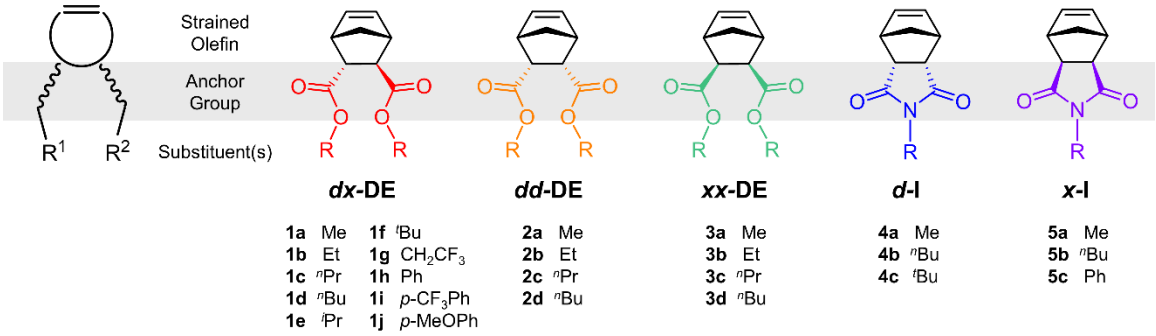

Scheme 2.3 highlights opportunities for monomer design. The polymerizable strained olefin, anchor group, and substituents can all be readily modified. Substituted norbornenes were selected for our study due to (1) the ease of modifying the

stereochemistry and functional groups and (2) the high ring strain, which disfavors unproductive [2+2] cycloreversion.[73] The importance of the anchor group in homopolymerization kinetics has been demonstrated for both discrete norbornenes[56,74] and more recently, *ω*-norbornenyl macromonomers.[65] In contrast, anchor group effects on the copolymerization of discrete monomers and macromonomers have not been studied. In order to investigate these effects, discrete substituted norbornenes with five different types of anchor groups were synthesized: *endo,exo*-diester (*dx*-DE, **1**), *endo,endo*-diester (*dd*-DE, **2**), *exo,exo*-diester (*xx*-DE, **3**), *endo*-imide (*d*-I, **4**), and *exo*-imide (*x*-I, **5**). For each anchor group, monomers with different substituents (R) were prepared, including for example homologous alkyl groups or *para*-substituted phenyl rings. All monomers can be prepared in high yields in one or two steps from commercially available starting materials. (Further synthetic details can be found in Appendix A-3.) These steric and electronic variations provide a diverse library of co-monomers for ROMP.

The homopolymerization kinetics of all monomers were studied under the same conditions (Section 2-3). Studying trends in k_{homo} with variations in steric and electronic structure guides monomer design. The first class of monomers studied herein features *endo,exo*-diester anchor groups (*dx*-DE). The homopolymerization kinetics of ten *dx*-DE monomers with different substituents were analyzed (**1a**–**1j**, Figure 2.10). The monomers were readily synthesized by esterification of commercially available norbornene *endo,exo*-dicarboxylic acid with the appropriate alcohol (**1a**–**d**, Scheme A.11). (For the synthesis of the bulkier monomers **1e**–**1j**, the acyl chloride derivatives were required; Scheme A.12.) In a series of monomers with homologous alkyl substituents (R = methyl, ethyl, *n*-propyl, *n*-butyl; **1a**–**d**), k_{homo} decreases with increasing substituent size. Increasing the steric bulk with isopropyl- and *tert*-butyl-substituted monomers (**1e**–**f**) further decreases k_{homo}. These results indicate that sterics clearly impact the homopolymerization kinetics: for example, the methyl-substituted monomer polymerizes over three times faster than the *tert*-butyl-substituted analogue (k_{homo} = 18.7 versus 5.36 M^{-1} s^{-1}). The effects of electronic variations were also studied. Monomers with ethyl (**1b**, 14.6 M^{-1} s^{-1}) and trifluoroethyl (**1g**, 10.5 M^{-1} s^{-1}) substituents polymerize at approximately the same rate. Comparison of *dx*-DE monomers with different *para*-substituted phenyl rings further reveals that the electronic effects are minor. *dx*-norbornenyl diphenylester (**1h**) has a larger k_{homo} (8.36 M^{-1} s^{-1}) than

monomers with either an electron-withdrawing *para*-trifluoromethyl group (**1i**, 5.14 M^{-1} s^{-1}) or an electron-donating *para*-methoxy group (**1j**, 7.76 M^{-1} s^{-1}). These electronic variations may exist too far away from the polymerizable olefin to affect k_{homo}. Modifying norbornene itself rather than the distal substituents (for example, by substituting oxanorbornene or otherwise changing the bridge position) may result in more apparent electronic effects.

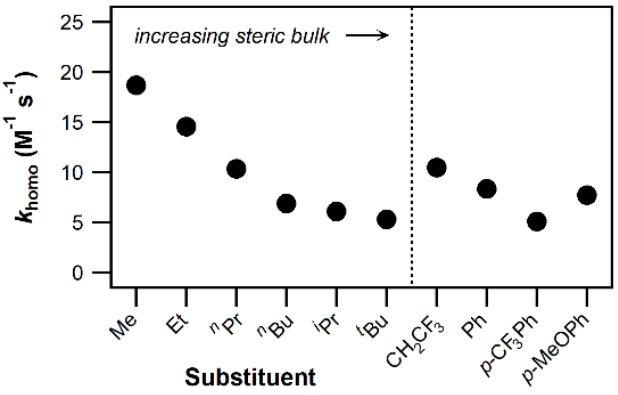

Figure 2.10: Homopolymerization rate constants (k_{homo}) for substituted *endo,exo*-norbornenyl diester monomers (left to right: **1a**–**j**). k_{homo} decreases with increasing steric bulk (R = Me to ^{t}Bu, **1a**–**f**). k_{homo} does not change significantly with electronic changes via fluorination (**1g**) or *para*-substitution of a phenyl ring (**1h**–**j**).

Changing the stereochemistry of the diester anchor groups further demonstrates the effects of steric variations on polymerization rates. (Synthetic details: Schemes A.13–A.14.) Comparing series with the same substituents (Figure 2.11A) indicates that *dx*-DE monomers (**1a**–**d**) all polymerize significantly faster than the corresponding *endo,endo* isomers (*dd*-DE, **2a**–**d**) and slightly slower than the corresponding *exo,exo* isomers (*xx*-DE, **3a**–**d**). For example, the measured k_{homo} for *dx*-norbornenyl dimethylester is 18.7 M^{-1} s^{-1}, while k_{homo} values for the *dd*-DE and *xx*-DE analogues are 2.24 M^{-1} s^{-1} and 30.8 M^{-1} s^{-1}, respectively. The same anchor group trend occurs for ethyl-, *n*-propyl-, and *n*-butyl-substituted norbornenyl diesters and is anticipated to be independent of the substituent.

In order to further examine the relationship between anchor groups and homopolymerization kinetics, norbornenyl monomers with *endo*-imide (*d*-I) and *exo*-imide (*x*-I) linkages were also synthesized (Schemes A.15–A.16). The *x*-I anchor group has been

widely incorporated in macromonomers toward the synthesis of bottlebrush polymers by grafting-through ROMP,[21,65,75-77] motivating our interest in imide-based diluents. Compared to diester anchor groups, imides are more rigid due to their fused rings and thereby change the monomer steric profile. The electronic character differs as well, since the electron density of an imide oxygen is typically greater than the electron density of an ester oxygen. The interplay of steric and electronic influences will be discussed further in Section 2-9.

Figure 2.11B compares k_{homo} for monomers with each of the five anchor groups. The *endo*/*exo* rate difference between *d*-I and *x*-I is magnified compared to the *endo*/*exo* rate differences observed among the diester-substituted monomers. The k_{homo} values for methyl-substituted *dd*-DE and *xx*-DE are 2.24 and 30.8 M^{-1} s^{-1} respectively, representing a tenfold rate difference; in comparison, the k_{homo} values for methyl-substituted *d*-I and *x*-I are 0.814 and 82.4 M^{-1} s^{-1} respectively, representing a *hundredfold* rate difference. Figure 2.11B also shows that the steric effects of the R group are smaller for *x*-I and *d*-I compared to the diester series. For monomers containing the same substituents, the following trend in k_{homo} is observed: *d*-I < *dd*-DE < *dx*-DE < *xx*-DE < *x*-I.

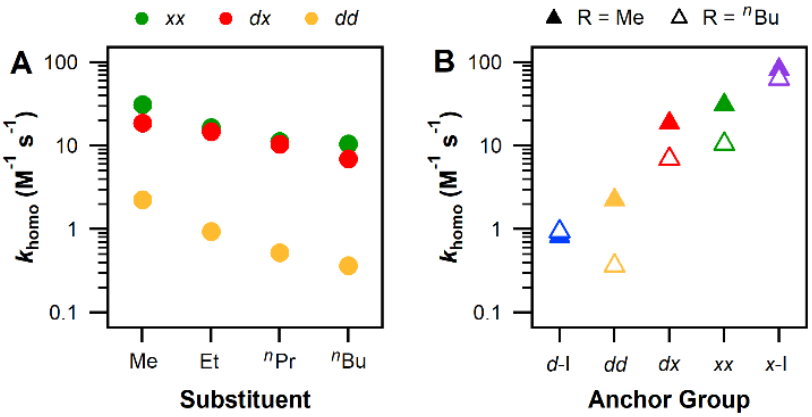

Figure 2.11: (*A*) Homopolymerization rate constants (k_{homo}) for monomers with *exo,exo*-diester (*xx*, green), *endo,exo*-diester (*dx*, red), and *endo,endo*-diester (*dd*, yellow) anchor groups. Comparison of k_{homo} for monomers with R = Me, Et, ^{n}Pr, and ^{n}Bu supports the steric influences of stereochemistry and substituent size. (*B*) k_{homo} for Me- and ^{n}Bu-substituted monomers with each of the five anchor groups; *endo*-imide (*d*-I, blue) and *exo*-imide (*x*-I, purple).

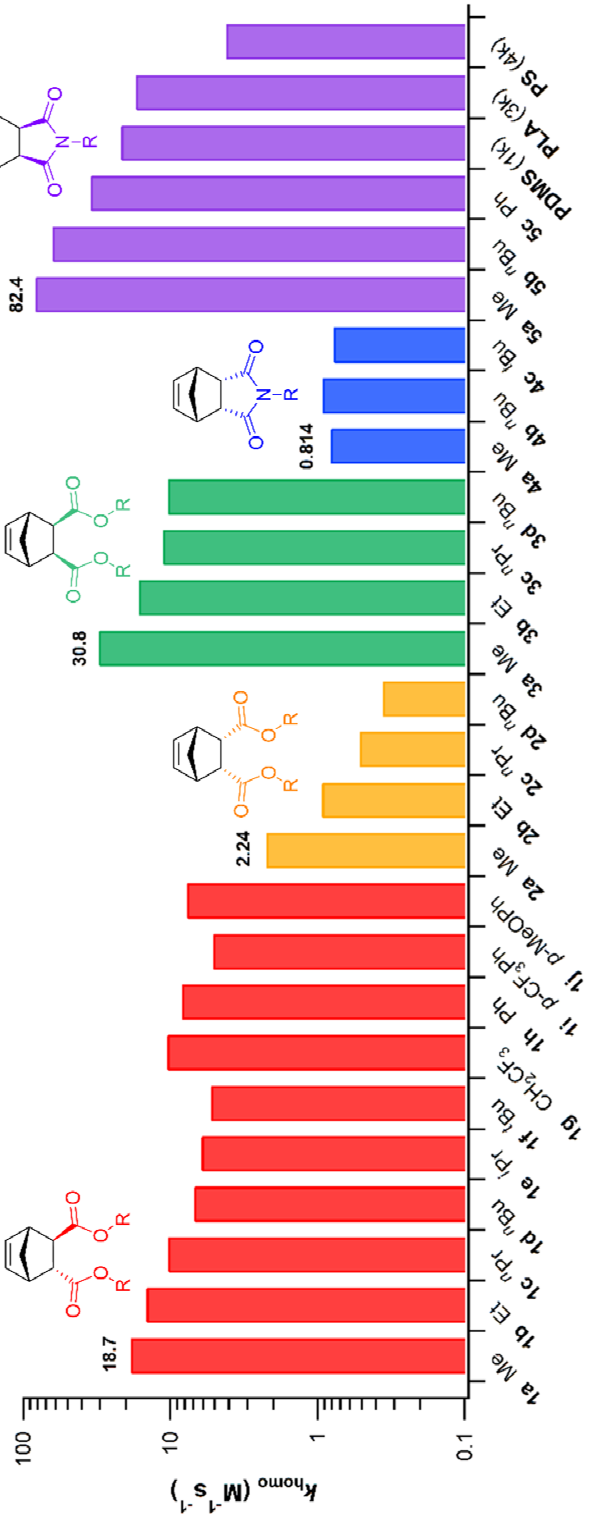

Figure 2.1: Plot of k_{homo} values for all monomers studied herein. The monomers are sorted according to their anchor groups: *left to right*: *endo,exo*-diester (red, **1a**–**j**), *endo,endo*-diester (yellow, **2a**–**d**), *exo,exo*-diester (green, **3a**–**d**), *endo*-imide (blue, **4a**–**c**), and *exo*-imide (purple, **5a**–**c** and macromonomers). k_{homo} values for methyl-substituted monomers are provided for comparison.

Figure 2.12 and Table A.2 summarize the homopolymerization kinetics for all monomers studied herein. Variations in the anchor groups and substituents afford a wide range of k_{homo} over two orders of magnitude, spanning 0.362 M^{-1} s^{-1} (**2d**) to 82.4 M^{-1} s^{-1} (**5a**). This library of monomers can be readily diversified by simple esterification reactions, providing a versatile platform for tuning the polymerization rates. Understanding the origin of trends in k_{homo} provides insight into the ROMP mechanism. While developing a complete mechanistic understanding is outside the scope of this study, we aim to identify key components of k_{homo} in order to facilitate applications of this method as well as future monomer design.

2-9 Origin of Rate Trends

Polymerization rates are determined by a combination of steric and electronic factors. Our results suggest that steric effects dominate: (1) In a series of monomers with homologous alkyl R groups, the electronic character is similar but k_{homo} decreases as the steric bulk increases (Figure 2.10). (2) k_{homo} is relatively insensitive to distal electronic variations (for example, via *para*-substitution of phenyl R groups, Figure 2.10). (3) k_{homo} decreases for *endo*-substituted monomers compared to the corresponding *exo* isomers (Figure 2.11). In agreement with this work, previous studies of the ROMP of norbornene derivatives have also observed that *endo* isomers polymerize more slowly than their *exo* counterparts.[74,78-81]

The observed rate trends could be motivated by a combination of factors, including but not limited to pyridine coordination, olefin coordination, cycloaddition, and formation of a six-membered chelate involving the ruthenium center and the ester- or imide-functionalized chain end.[82] In order to deconvolute these potential contributions to k_{homo}, we examined the mechanism of ROMP. Based on previously reported results for related phosphine-based catalysts,[83-85] we propose a dissociative pathway (Figure 2.13) in which pyridine dissociation ($K_{eq,1} = k_1/k_{-1}$, $K_{eq,2} = k_2/k_{-2}$) generates a 14-electron intermediate (b) that can coordinate with a free olefin (c, $K_{eq,3} = k_3/k_{-3}$). The olefin adduct then undergoes cycloaddition (k_4) to form a metallacyclobutane intermediate. Subsequent cycloreversion yields a P_{n+1} alkylidene and regenerates the 14-electron species. From a Van't Hoff analysis, Guironnet and coworkers recently reported an equilibrium constant $K_{eq,1} = k_1/k_{-1}$

= 0.5 M in CD_2Cl_2 at 298 K.[86] In agreement with this work, we observed a similar $K_{eq,1}$ value from ^{1}H NMR pyridine titration experiments (0.25 M, Figure A.6. The large $K_{eq,1}$ value indicates that >99.8% of the precatalyst **G3** exists as the monopyridine adduct in solution under the conditions employed in our homo- and copolymerization studies ($[\mathbf{G3}]_0$ = 0.5 mM). As a result, the concentration of free pyridine is approximately equal to the initial concentration of **G3** (*i.e.,* [pyr] ≈ $[\mathbf{G3}]_0$). We derived a simplified rate expression corresponding to a proposed dissociative ROMP pathway in which olefin coordination is the rate-limiting step (Appendix A-7.2):[87]

$$-\frac{d[M]_t}{dt} = k_{homo}[\mathbf{G3}]_0[M]_t \approx \frac{K_{eq,2}k_3}{K_{eq,2}+[pyr]}[\mathbf{G3}]_0[M]_t \qquad \text{Eq. 2-8}$$

In this rate expression, $K_{eq,2}$ corresponds to dissociation of the second pyridine and is affected by the identity of the alkylidene ligand. At high catalyst concentrations ([pyr] >> $K_{eq,2}$), a pseudo-zeroth-order dependence on $[\mathbf{G3}]_0$ is observed.[86] At low catalyst concentrations however, we observed a rate dependence on $[\mathbf{G3}]_0$ for monomers **5a** and **5b** (Figure A.7). Collectively, these kinetic analyses are consistent with a dissociative pathway.[88]

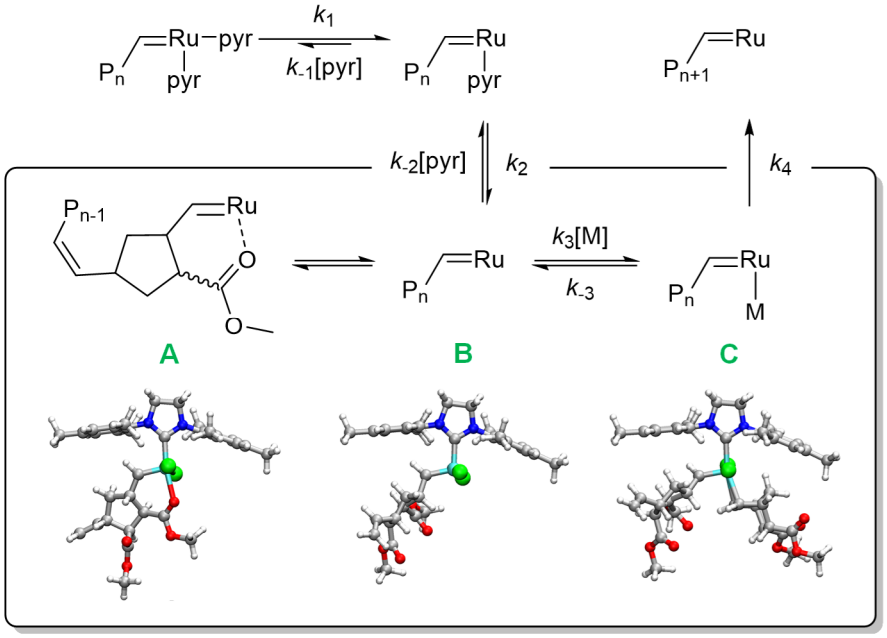

Figure 2.13: Proposed dissociative ROMP pathway for **G3**. The DFT-optimized structures of three catalytically relevant ruthenium catalyst species are shown: (*A*) six-membered Ru−O chelate, (*B*) 14-electron vacant species, and (*C*) olefin adduct.

Density functional theory (DFT) methods were employed to address potential chelation effects. Chelation sequesters the catalyst in an unproductive form (Figure 2.13A) and therefore slows the polymerization rate.[89] For methyl-substituted *endo,endo*- and *exo,exo*-norbornenyl diesters (**2a** and **3a**, respectively), the ground-state potential energy surfaces corresponding to one productive ROMP cycle were computed (Figure 2.14). The relative free energies at 298 K (ΔG) indicate that formation of the six-membered chelate is more favorable for the *endo* isomer ($\Delta\Delta G_{chelate}$ = 9.64 kcal mol^{-1}) than for the *exo* isomer ($\Delta\Delta G_{chelate}$ = 5.87 kcal mol^{-1}). The calculated free energies corresponding to olefin coordination to the vacant species, $\Delta\Delta G_{binding}$, are similar for the *endo* and *exo* isomers (8.86 and 8.91 kcal mol^{-1}, respectively). These results indicate that disruption of chelation by olefin binding should be more favorable for *exo* isomers than *endo* isomers (by 3.72 kcal mol^{-1}). This disparity provides a plausible motive for the observed *endo*/*exo* rate differences (k_{homo} = 30.8 M^{-1} s^{-1} for **3a**, 2.24 M^{-1} s^{-1} for **2a**). These results are consistent with previous reports on the ROMP of discrete norbornenyl monomers with similar ruthenium catalysts[82,84,90] and are anticipated to be valid whether olefin coordination (k_3 << k_4) or cycloaddition (k_3 >> k_4) is the rate-limiting step.[91] Insights into the rate trends from mechanistic studies help identify important elements of monomer design and, therefore, opportunities for controlled copolymerization.

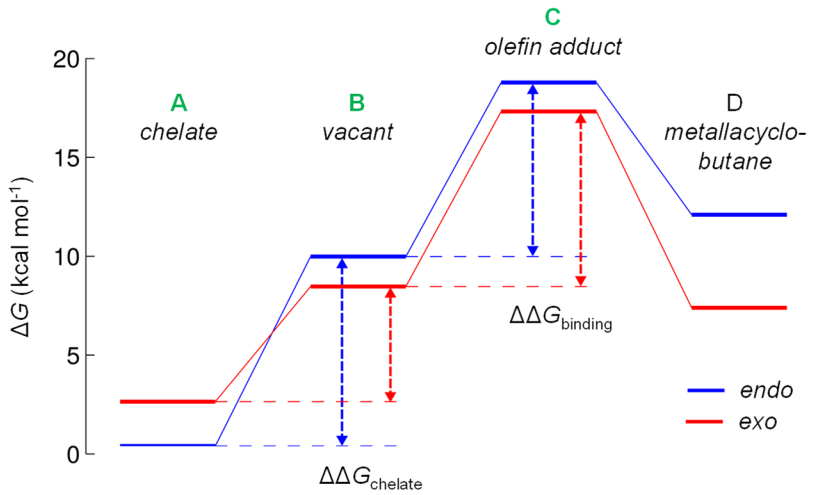

Figure 2.14: DFT-calculated free energy diagram corresponding to one ROMP cycle for *endo*- (**2a**, blue) and *exo*-substiuted (**3a**, red) norbornenyl monomers. The following intermediates were calculated: (*A*) six-membered Ru–O chelate, (*B*) 14-electron vacant species, (*C*) olefin adduct, and (*D*) metallacyclobutane. See also Figure 2.13.

2-10 Copolymerization Kinetics

In order to analyze the copolymerization kinetics of a macromonomer and a discrete co-monomer, we adapted the Mayo-Lewis terminal model was adapted for **G3**-catalyzed ROMP (Section 2-4).[67] The conversion over time of all species (*i.e.*, monomers M_1 and M_2 and propagating alkylidenes M_1* and M_2*) can be described by a system of four ordinary differential equations (Eqs. 2-2 to 2-5). Non-linear least squares regression (Section 2-4) was used to fit the instantaneous monomer concentrations over the entire course of the copolymerization. Finding the best numerical solutions for the cross-propagation rates k_{12} and k_{21} enables determination of the reactivity ratios, $r_1 = k_{11}/k_{12}$ and $r_2 = k_{22}/k_{21}$.

The relative reactivity, captured by r_1 and r_2, determines the polymer sequence. r_1 and r_2 can be tuned by building on insights into homopolymerization rate trends. Monomer design ultimately enables architecture design: for a polymerizable macromonomer with any side chain chemistry, a discrete co-monomer can be selected among those in Scheme 2.3 or otherwise designed to target desired backbone sequences. In turn, control over the backbone sequence directly controls side chain distribution. We will first discuss general trends and opportunities for copolymerization, then outline potential implications for polymer architectures by design.

In order to study the impact of monomer structure on the copolymerization kinetics, we selected 13 diluents and copolymerized each with the same ω-norbornenyl macromonomer (**PLA**, M_n = 3230 g/mol) (Figure 2.15A). Figure 2.15B arranges these discrete co-monomers in order of increasing k_{22}. For all copolymerization experiments, the total backbone degree of polymerization (N_{bb}) and monomer feed ratio (f) were fixed: given x equivalents of the diluent and y equivalents of **PLA** relative to 1 equivalent of **G3**, $N_{bb} = x + y \approx 200$ and $f = x/y \approx 1$. The copolymerization conditions, including monomer and catalyst concentrations, were identical to those for the homopolymerization experiments described in Section 2-3: $[M_1]_0 = [M_2]_0 = 50$ mM, $[\mathbf{G3}]_0 = 0.5$ mM.[92] The kinetics were monitored in the same way as the homopolymerization kinetics, *i.e.*, by quenching aliquots of the polymerization mixture. The instantaneous concentrations of the macromonomer and diluent were determined by integrating the olefin resonances in ^{1}H NMR spectra, and k_{12} and k_{21} were obtained by non-linear least squares regression. SEC data for all

copolymers indicate low dispersities ($Đ < 1.1$) and similar molecular weights (Figure 2.16, Table A.3).

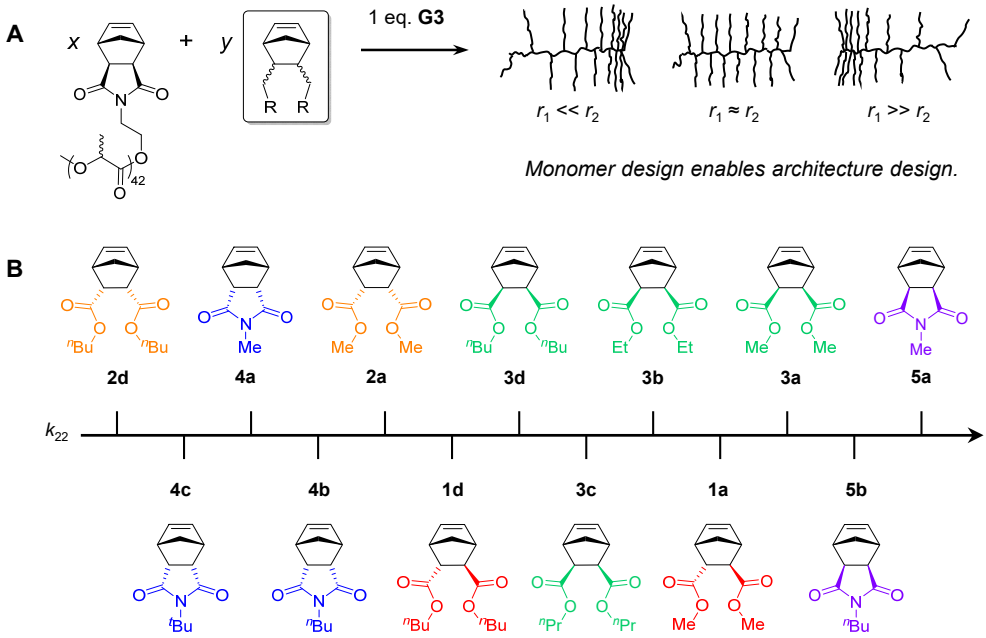

Figure 2.15: (*A*) Copolymerization scheme: the same macromonomer (**PLA**, M_1) was copolymerized with 13 different diluents (M_2). The feed ratio ($x/y = 1$) and total backbone length ($x + y = 200$) were fixed. (*B*) M_2 arranged in order of increasing k_{22}.

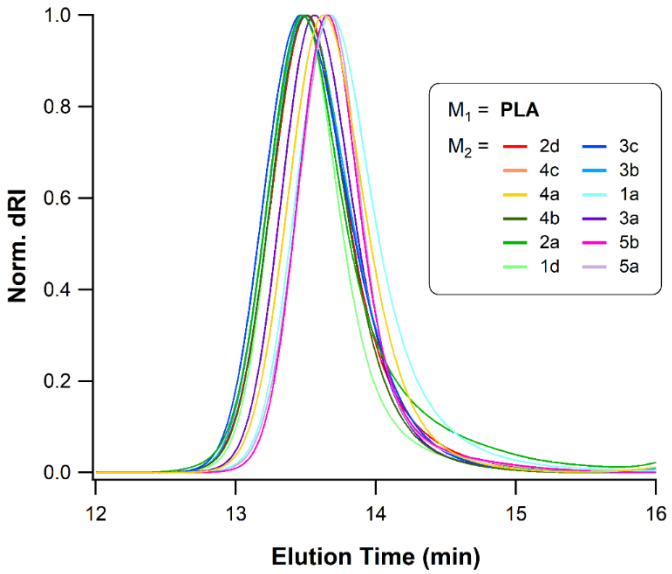

Figure 2.16: SEC traces for **PLA** + diluent copolymerizations at full conversion.

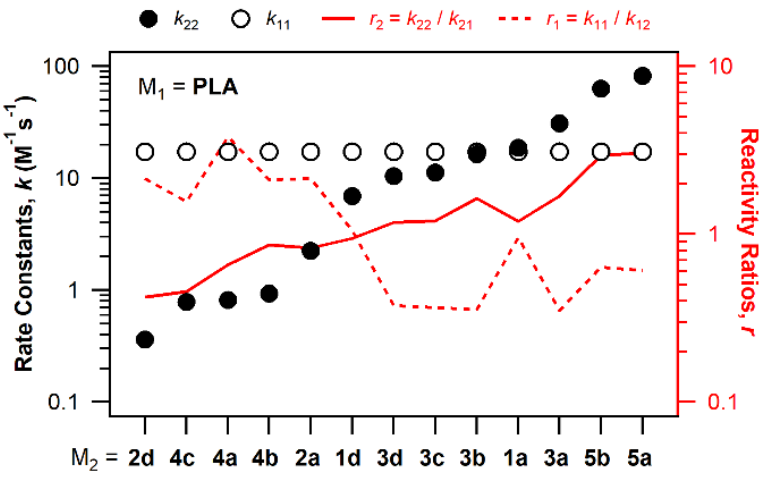

Figure 2.17: PLA/diluent copolymerization data. Left axis, black: self-propagation rate constants (k_{22}: filled circles, k_{11}: open circles). Right axis, red: reactivity ratios (r_2: solid line, r_1: dotted line)

Figure 2.17 shows the self-propagation rate constants (k_{11}, k_{22}) and reactivity ratios (r_1, r_2) for the copolymerization of **PLA** (M_1) with different diluents (M_2). (All data, including the cross-propagation rate constants k_{12} and k_{21}, are compiled in Table A.4.) k_{11} is constant throughout the series (= 17.2 $M^{-1}\,s^{-1}$) since M_1 is the same in each co-monomer pair, while k_{22} varies over a wide range due to anchor group and substituent effects (**2d**: 0.362 $M^{-1}\,s^{-1}$ to **5a**: 82.4 $M^{-1}\,s^{-1}$). As k_{22} increases, r_2 also increases. The magnitude of r_2 reflects the reactivity of the propagating alkylidene M_2* toward free M_1 and M_2.[93] In the case that $r_2 < 1$, for example when **PLA** is copolymerized with *dd*-DE or *d*-I diluents (**2d** to **2a**, $0.4 < r_2 < 0.9$), M_2* preferentially adds M_1. In the opposite case $r_2 > 1$, for example when **PLA** is copolymerized with *dx*-DE, *xx*-DE, or *x*-I diluents (**3d** to **5a**, $1.2 < r_2 < 3.1$), M_2* preferentially adds M_2 instead. In other words, if a diluent is the terminal unit of the propagating species, the probability of incorporating either a macromonomer or another diluent reflects the difference between the homopolymerization rate constants: when $k_{22} < k_{11}$, $r_2 < 1$ and M_2* favors *macromonomer* addition; on the other hand, when $k_{22} > k_{11}$, $r_2 > 1$ and M_2* favors *diluent* addition.[94] Translating these trends to the copolymer sequence also requires examination of r_1, which reflects consumption of the other propagating species M_1*. Figure 2.17 shows that, as k_{22} increases, r_1 generally decreases, opposite the trend observed for r_2. These observations suggest that both M_1* and M_2* (1) favor incorporating M_2 when $k_{22} \gtrsim k_{11}$ and (2) favor incorporating M_1 when $k_{22} < k_{11}$. In other

words, both cross-propagation terms (k_{12} and k_{21}) are functions of the incoming olefin (to first order) and appear relatively insensitive to the nature of the pendant chain.

We note that, while r_1 generally decreases with increasing k_{22}, the trend is not monotonic. These results highlight the additional complexity that copolymerization introduces. While informative, the difference between the homopolymerization rate constants ($k_{11}-k_{22}$) is not a universal predictor for the values of r_1 and r_2 (nor therefore the copolymer sequence). For example, when **PLA** is copolymerized with a *xx*-DE diluent, r_2 varies but r_1 remains the same (= 0.36 ± 0.02), regardless of whether $k_{22} < k_{11}$ (**3d**, **3c**, and **3b**) or $k_{22} > k_{11}$ (**3a**). Meanwhile, when **PLA** is copolymerized with the *dx*-DE analogue of **3a** (*i.e.*, **1a**), the self-propagation rates are equal ($k_{22} = k_{11}$) and both r_1 and r_2 are approximately equal to 1. These observations suggest that the key interactions identified in our study of diluent homopolymerization rate trends do not fully capture the relative reactivity upon copolymerization. The individual second-order rate constants (k_{11}, k_{12}, k_{21}, k_{22}) are affected by both (1) pyridine binding ($K_{eq,2}$) and (2) chelation and olefin binding (k_3). Both those terms are inherently dictated by the identities of the approaching olefin monomer and the propagating alkylidene. While elucidating the origin of copolymerization rate trends is outside the scope of this report, we note that the large disparity between the molecular weights of the PLA macromonomer and diluents (10- to 20-fold) likely plays a significant role in the departure from simple chain-end control. Under the copolymerization conditions (rapid stirring in dilute solution), simple diffusion of free monomers to the catalyst active site is not expected to limit propagation. However, beyond the anchor group and substituent effects outlined for discrete diluents, the presence of polymeric side chains in proximity to the metal center should amplify steric congestion. Excluded volume interactions and solvent quality may further affect the steric and electronic environment around the propagating metal center.

2-11 Tuning Graft Polymer Architecture

Monitoring the copolymerization kinetics enables determination of the instantaneous composition and therefore the graft polymer architecture. Using the experimentally determined rate constants, the probability of incorporating either a diluent or a macromonomer at any point in the growing chain can be simulated (Section 2-6).[67]

Figure 2.18 plots these probabilities as a function of the total conversion for several **PLA**/diluent pairs. If $r_1 > r_2$, gradient sequences are obtained. The copolymers are rich in M_1 at early conversions and rich in M_2 at later conversions, producing tapered side chain distributions (*e.g.*, **PLA** + **4a**, Figure 2.18A). If $r_1 \approx r_2 \approx 1$, the copolymer backbone sequence is approximately random and therefore the side chains are uniformly distributed (*e.g.* **PLA** + **1a**, Figure 2.18B). Lastly, if $r_1 < r_2$, the inverse-tapered graft polymers are obtained, which are rich in M_2 at early conversions and rich in M_1 at later conversions (*e.g.*, **PLA** + **5a**, Figure 2.18C).

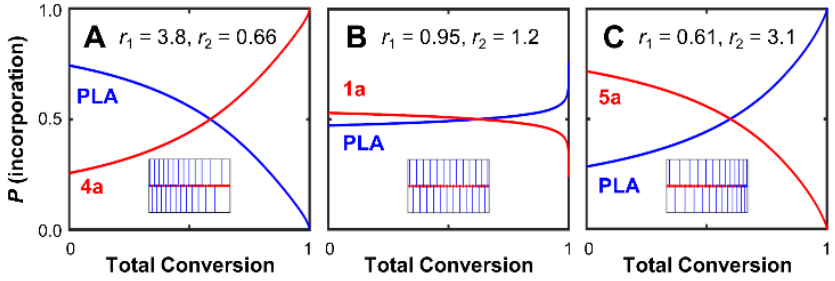

Figure 2.18: Simulated sequences and (inset) graft polymer architectures for the copolymerization of **PLA** with different diluents: (*A*) **4a**, (*B*) **1a**, or (*C*) **5a**. For ease of visualization, the simulated structures show fully extended side chains and backbones.

The ROMP copolymerization strategy outlined herein provides a general approach to architecture design for any side chain chemistry. In principle, given any polymerizable macromonomer, a diluent can be designed to access any desired sequence. Although the magnitudes of r_1 and r_2 cannot presently be predicted *de novo*, insights into the relationships among r_1, r_2, and diluent structure should guide the selection of appropriate macromonomer/diluent pairs. In order to further illustrate these design principles, the copolymerization kinetics of various diluents with either a **PDMS** (M_n = 1280 g/mol) or **PS** (M_n = 3990 g/mol) macromonomer were also studied. **PDMS** and **PS** polymerize faster (k_{11} = 21.6 M^{-1} s^{-1}) and slower (k_{11} = 4.18 M^{-1} s^{-1}) than **PLA**, respectively. The selected diluents all homopolymerize slower than **PDMS** ($k_{22} < k_{11}$, with the exception of **3a**) and faster than **PS** ($k_{22} > k_{11}$). The self-propagation rate constants and reactivity ratios are provided in Figure 2.19 and compiled in Tables A.5–A.6. SEC data are provided in Tables A.7–A.8 and Figures A.8–A.9.

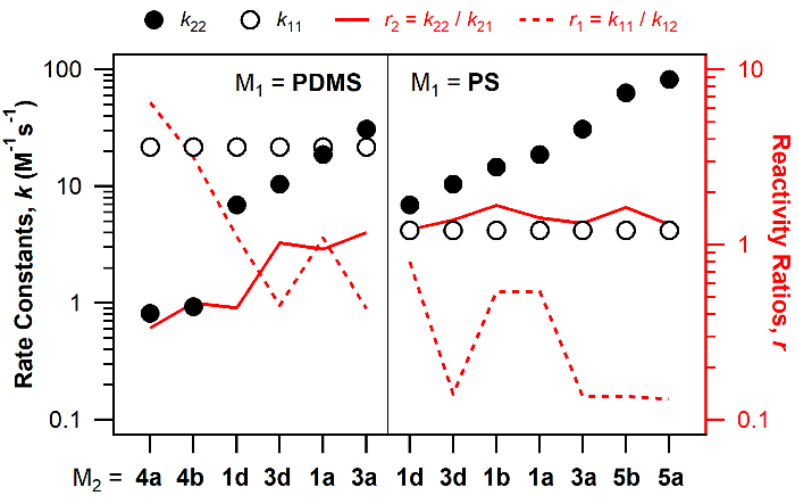

Figure 2.19: Data for the copolymerization of M_1 = **PDMS** (left) or **PS** (right) with different diluents. Left axis, black: self-propagation rate constants (k_{22}: filled circles, k_{11}: open circles). Right axis, red: reactivity ratios (r_2: solid line, r_1: dotted line).

Copolymerizations of **PDMS** with each of the selected diluents generally follow the same trends outlined for **PLA**/diluent copolymerizations. As k_{22} increases while k_{11} remains constant, r_2 increases and r_1 decreases. In other words, as k_{22} increases, both M_1* and M_2* increasingly favor incorporating M_2 instead of M_1. The *xx*-DE diluents (**3a**, **3d**) are again outliers, leading to smaller values of r_1 than diluents with any other anchor group. As a result, at least for copolymerizations with **PDMS** or **PLA** macromonomers, the *xx*-DE anchor group inherently favors gradient sequences that are M_2-rich at early conversions and M_1-rich at later conversions. Copolymerizations of **PS** with any of the selected diluents reveal a similar kinetic preference for gradient sequences. Unlike copolymerizations with either **PLA** or **PDMS**, regardless of the relative magnitude of k_{22} ($2.7 < k_{22}–k_{11} < 78$ M^{-1} s^{-1}), r_2 remains constant (≈ 1). The constant magnitude of r_2 suggests that M_2* displays similar reactivity toward **PS** and any diluent. Meanwhile, since M_1* favors incorporating M_2 ($r_1 < 1$), gradient sequences result.

The copolymerization kinetics for **PLA**, **PDMS**, and **PS** collectively illustrate how different diluents can be used to control the graft polymer architecture. The magnitudes of r_1 and r_2 determine the backbone sequence, which can be alternating ($r_1 \approx r_2 \approx 0$), blocky ($r_1, r_2 >> 1$), gradient ($r_1 >> r_2$ or $r_1 << r_2$), or random ($r_1 \approx r_2 \approx 1$).[93] The backbone sequence in turn directly determines the side chain distribution. Figure 2.20 illustrates the wide range

of distributions obtained by copolymerizing **PLA**, **PDMS**, or **PS** with selected diluents. The relative reactivities of the macromonomers and diluents are interpreted in terms of the quotient r_1/r_2, which reflects the kinetic preference for the chain end (either M_1* or M_2*) to incorporate M_1 over M_2.

PLA/diluent copolymerizations obtain r_1/r_2 ranging from 0.20 (**PLA** + **5a**) to 5.8 (**PLA** + **4a**). Copolymerizing **PDMS** with **4a**, one of the slowest-polymerizing diluents studied herein, produces a remarkably large difference between r_1 and r_2: $r_1/r_2 = 19$. This large disparity in reactivity results in a highly gradient – potentially even blocky – distribution of side chains. Since $r_1 >> r_2$, the graft polymers are densely grafted (*i.e.*, rich in M_1) at early conversions and loosely grafted (*i.e.*, rich in M_2) at later conversions. Copolymerizing **PS** with **5b**, one of the fastest-polymerizing diluents introduced in this report, also affords a wide gap in reactivity: $r_1/r_2 = 0.084$. Compared to **PDMS** + **4a**, the inverse-tapered sequence is obtained. The ability to invert the gradient direction may not affect the properties of homopolymers, but it is valuable in the design of block polymers and other multicomponent materials. In Chapter 3, we will demonstrate the physical consequences of varying the sequence distribution in the context of block polymer self-assembly.

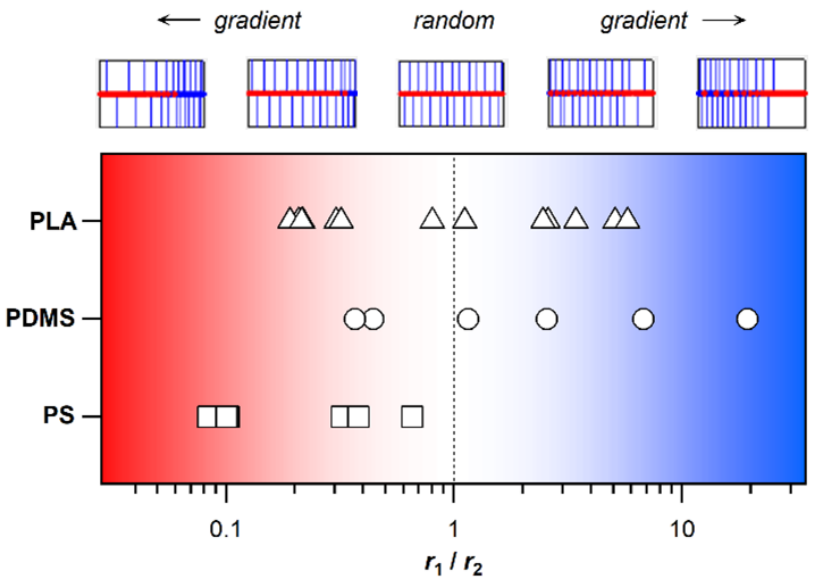

Figure 2.20: Reactivity ratio map. The copolymerization kinetics studied for **PLA**, **PDMS**, and **PS** are interpreted in terms of the quotient r_1/r_2, plotted on the x-axis. For ease of visualization, the simulated structures show fully extended side chains and backbones.

2-12 Conclusion

Grafting-through ring-opening metathesis polymerization (ROMP) provides a versatile strategy for the design and synthesis of polymers with tailored side chain distributions. Controlled copolymerization of an ω-norbornenyl macromonomer and a discrete norbornenyl diluent constructs graft architectures through the backbone; as a result, the backbone sequence directly dictates the side chain distribution. Since tuning the backbone sequence requires changing the relative reactivity of the co-monomers, we first investigated steric and electronic effects on the homopolymerization kinetics of 23 diluents. Varying the stereochemistry, anchor groups, and substituents varies the homopolymerization rate constants over two orders of magnitude ($0.36\ M^{-1}\ s^{-1} \leq k_{homo} \leq 82\ M^{-1}\ s^{-1}$), reflecting a wide scope of monomer reactivity. These small-molecule monomers can be readily prepared and diversified, providing a convenient library for future development. In order to provide further guidance, we identified rate trends and studied their origins through complementary mechanistic studies. Density functional theory (DFT) calculations suggest that formation of a Ru–O six-membered chelate (which sequesters the catalyst in an unproductive form) is significantly different for *endo* and *exo* isomers. Future studies will expand our understanding of the ROMP mechanism for both diluents and macromonomers. Other factors that could affect the ROMP kinetics, including for example solvent quality and additives, will also be explored.

Building on these results, we studied the copolymerization kinetics of selected diluents and a poly($_{D,L}$-lactide) (**PLA**), polydimethylsiloxane (**PDMS**), or polystyrene (**PS**) macromonomer. The co-monomer concentrations were monitored by ^{1}H NMR, and the cross-propagation rate constants were calculated by non-linear least squares regression based on the Mayo-Lewis terminal model. Trends involving the measured self-propagation rate constants and the calculated reactivity ratios (r_1 and r_2) were identified. In general, for the 26 co-monomer pairs studied, the greater the difference between homopolymerization rates, the greater the gradient tendency ($r_1/r_2 >> 1$ or $r_1/r_2 << 1$). The backbone sequence – and therefore the polymer architecture – can be tailored simply by choosing the appropriate diluent among the library introduced herein or by designing an appropriate monomer. We note that, at present, *de novo* prediction of the reactivity ratios from the macromonomer and diluent chemical structures is not possible. However, we anticipate that the versatility

of this design strategy, coupled with the broad functional group tolerance of ROMP and its living character, should enable the design and synthesis of graft polymers with almost any desired graft chemistry and graft distribution. The design strategy outlined herein provides extensive customizability in terms of polymer structure and functionality, illuminating new opportunities for molecular and materials design.

2-13 References

(1) Hadjichristidis, N.; Pitsikalis, M.; Pispas, S.; Iatrou, H. *Chem. Rev.* **2001**, *101*, 3747–3792.
(2) Polymeropoulos, G.; Zapsas, G.; Ntetsikas, K.; Bilalis, P.; Gnanou, Y.; Hadjichristidis, N. *Macromolecules* **2017**, *50*, 1253–1290.
(3) Matyjaszewski, K.; Tsarevsky, N. V. *Nature Chem.* **2009**, *1*, 276–288.
(4) Bates, C. M.; Bates, F. S. *Macromolecules* **2017**, *50*, 3–22.
(5) Kikuchi, M.; Nakano, R.; Jinbo, Y.; Saito, Y.; Ohno, S.; Togashi, D.; Enomoto, K.; Narumi, A.; Haba, O.; Kawaguchi, S. *Macromolecules* **2015**, *48*, 5878–5886.
(6) Liang, H.; Cao, Z.; Wang, Z.; Sheiko, S. S.; Dobrynin, A. V. *Macromolecules* **2017**, *50*, 3430–3437.
(7) Paturej, J.; Sheiko, S. S.; Panyukov, S.; Rubinstein, M. *Sci. Adv.* **2016**, *2*, e1601478.
(8) Rathgeber, S.; Pakula, T.; Wilk, A.; Matyjaszewski, K.; Beers, K. L. *J. Chem. Phys.* **2005**, *122*, 124904.
(9) Abbasi, M.; Faust, L.; Riazi, K.; Wilhelm, M. *Macromolecules* **2017**, *50*, 5964–5977.
(10) Dalsin, S. J.; Hillmyer, M. A.; Bates, F. S. *Macromolecules* **2015**, *48*, 4680–4691.
(11) Hu, M.; Xia, Y.; McKenna, G. B.; Kornfield, J. A.; Grubbs, R. H. *Macromolecules* **2011**, *44*, 6935–6943.
(12) Daniel, W. F. M.; Burdynska, J.; Vatankhah-Varnoosfaderani, M.; Matyjaszewski, K.; Paturej, J.; Rubinstein, M.; Dobrynin, A. V.; Sheiko, S. S. *Nat. Mater.* **2016**, *15*, 183–189.
(13) Mai, D. J.; Marciel, A. B.; Sing, C. E.; Schroeder, C. M. *ACS Macro Lett.* **2015**, *4*, 446–452.
(14) Kapnistos, M.; Kirkwood, K. M.; Ramirez, J.; Vlassopoulos, D.; Leal, L. G. *J. Rheol.* **2009**, *53*, 1133–1153.
(15) Read, D. J.; Auhl, D.; Das, C.; den Doelder, J.; Kapnistos, M.; Vittorias, I.; McLeish, T. C. B. *Science* **2011**, *333*, 1871–1874.
(16) Jeong, S. H.; Kim, J. M.; Baig, C. *Macromolecules* **2017**, *50*, 4491–4500.
(17) Liberman-Martin, A. L.; Chu, C. K.; Grubbs, R. H. *Macromol. Rapid Commun.* **2017**, *38*, 1700058.
(18) Runge, M. B.; Bowden, N. B. *J. Am. Chem. Soc.* **2007**, *129*, 10551–10560.
(19) Sveinbjörnsson, B. R.; Weitekamp, R. A.; Miyake, G. M.; Xia, Y.; Atwater, H. A.; Grubbs, R. H. *Proc. Natl. Acad. Sci. U.S.A.* **2012**, *109*, 14332–14336.
(20) Qiu, L. Y.; Bae, Y. H. *Biomaterials* **2007**, *28*, 4132–4142.
(21) Johnson, J. A.; Lu, Y. Y.; Burts, A. O.; Lim, Y.-H.; Finn, M. G.; Koberstein, J. T.; Turro, N. J.; Tirrell, D. A.; Grubbs, R. H. *J. Am. Chem. Soc.* **2011**, *133*, 559–566.

(22) Bhattarai, N.; Ramay, H. R.; Gunn, J.; Matsen, F. A.; Zhang, M. *J. Control. Release* **2005**, *103*, 609–624.
(23) Bates, C. M.; Chang, A. B.; Momčilović, N.; Jones, S. C.; Grubbs, R. H. *Macromolecules* **2015**, *48*, 4967–4973.
(24) Bates, C. M.; Chang, A. B.; Schulze, M. W.; Momčilović, N.; Jones, S. C.; Grubbs, R. H. *J. Polym. Sci., Part B: Polym. Phys.* **2016**, *54*, 292–300.
(25) Jiang, F.; Wang, Z.; Qiao, Y.; Wang, Z.; Tang, C. *Macromolecules* **2013**, *46*, 4772–4780.
(26) Zhang, J.; Schneiderman, D. K.; Li, T.; Hillmyer, M. A.; Bates, F. S. *Macromolecules* **2016**, *49*, 9108–9118.
(27) Ma, H.; Wang, Q.; Sang, W.; Han, L.; Liu, P.; Chen, J.; Li, Y.; Wang, Y. *Macromol. Rapid Commun.* **2015**, *36*, 726–732.
(28) Prudnikova, K.; Yucha, R. W.; Patel, P.; Kriete, A. S.; Han, L.; Penn, L. S.; Marcolongo, M. S. *Biomacromolecules* **2017**, *18*, 1713–1723.
(29) Noel, A.; Borguet, Y. P.; Wooley, K. L. *ACS Macro Lett.* **2015**, *4*, 645–650.
(30) Wang, Q.; Ma, H.; Sang, W.; Han, L.; Liu, P.; Shen, H.; Huang, W.; Gong, X.; Yang, L.; Wang, Y.; Li, Y. *Polym. Chem.* **2016**, *7*, 3090–3099.
(31) Grubbs, R. B.; Hawker, C. J.; Dao, J.; Fréchet, J. M. J. *Angew. Chem., Int. Ed.* **1997**, *36*, 270–272.
(32) Shinoda, H.; Matyjaszewski, K. *Macromolecules* **2001**, *34*, 6243–6248.
(33) Börner, H. G.; Duran, D.; Matyjaszewski, K.; da Silva, M.; Sheiko, S. S. *Macromolecules* **2002**, *35*, 3387–3394.
(34) Lee, H.-i.; Matyjaszewski, K.; Yu, S.; Sheiko, S. S. *Macromolecules* **2005**, *38*, 8264–8271.
(35) Sutthasupa, S.; Shiotsuki, M.; Sanda, F. *Polym. J.* **2010**, *42*, 905–915.
(36) Bielawski, C. W.; Grubbs, R. H. *Prog. Polym. Sci.* **2007**, *32*, 1–29.
(37) Leitgeb, A.; Wappel, J.; Slugovc, C. *Polymer* **2010**, *51*, 2927–2946.
(38) Zhang, B.; Gröhn, F.; Pedersen, J. S.; Fischer, K.; Schmidt, M. *Macromolecules* **2006**, *39*, 8440–8450.
(39) Sheiko, S. S.; Sumerlin, B. S.; Matyjaszewski, K. *Prog. Polym. Sci.* **2008**, *33*, 759–785.
(40) Zhang, M.; Müller, A. H. E. *J. Polym. Sci., Part A: Polym. Chem.* **2005**, *43*, 3461–3481.
(41) Lee, H.-i.; Pietrasik, J.; Sheiko, S. S.; Matyjaszewski, K. *Prog. Polym. Sci.* **2010**, *35*, 24–44.
(42) Peng, S.; Bhushan, B. *RSC Adv.* **2012**, *2*, 8557–8578.
(43) Pesek, S. L.; Li, X.; Hammouda, B.; Hong, K.; Verduzco, R. *Macromolecules* **2013**, *46*, 6998–7005.
(44) Pesek, S. L.; Xiang, Q.; Hammouda, B.; Verduzco, R. *J. Polym. Sci., Part B: Polym. Phys.* **2017**, *55*, 104–111.
(45) Gerle, M.; Fischer, K.; Roos, S.; Müller, A. H. E.; Schmidt, M.; Sheiko, S. S.; Prokhorova, S.; Möller, M. *Macromolecules* **1999**, *32*, 2629–2637.
(46) Al Samak, B.; G. Carvill, A.; J. Rooney, J.; M. Thompson, J. *Chem. Commun.* **1997**, 2057–2058.
(47) Elling, B. R.; Xia, Y. *J. Am. Chem. Soc.* **2015**, *137*, 9922–9926.

(48) Sutthasupa, S.; Shiotsuki, M.; Masuda, T.; Sanda, F. *J. Am. Chem. Soc.* **2009**, *131*, 10546–10551.
(49) Jeong, H.; John, J. M.; Schrock, R. R. *Organometallics* **2015**, *34*, 5136–5145.
(50) Jang, E. S.; John, J. M.; Schrock, R. R. *ACS Cent. Sci.* **2016**, *2*, 631–636.
(51) Jha, S.; Dutta, S.; Bowden, N. B. *Macromolecules* **2004**, *37*, 4365–4374.
(52) Xia, Y.; Olsen, B. D.; Kornfield, J. A.; Grubbs, R. H. *J. Am. Chem. Soc.* **2009**, *131*, 18525–18532.
(53) Li, Z.; Zhang, K.; Ma, J.; Cheng, C.; Wooley, K. L. *J. Polym. Sci., Part A: Polym. Chem.* **2009**, *47*, 5557–5563.
(54) Lu, H.; Wang, J.; Lin, Y.; Cheng, J. *J. Am. Chem. Soc.* **2009**, *131*, 13582–13583.
(55) Zhang, H.; Zhang, Z.; Gnanou, Y.; Hadjichristidis, N. *Macromolecules* **2015**, *48*, 3556–3562.
(56) Moatsou, D.; Hansell, C. F.; O'Reilly, R. K. *Chem. Sci.* **2014**, *5*, 2246–2250.
(57) Love, J. A.; Morgan, J. P.; Trnka, T. M.; Grubbs, R. H. *Angew. Chem. Int. Ed.* **2002**, *41*, 4035–4037.
(58) Trzaskowski, B.; Grela, K. *Organometallics* **2013**, *32*, 3625–3630.
(59) Mayo, F. R.; Lewis, F. M. *J. Am. Chem. Soc.* **1944**, *66*, 1594–1601.
(60) Mayo, F. R.; Walling, C. *Chem. Rev.* **1950**, *46*, 191–287.
(61) Fineman, M.; Ross, S. D. *J. Polym. Sci.* **1950**, *5*, 259–262.
(62) Kelen, T.; Tüdös, F. *Journal of Macromolecular Science, Chemistry* **1975**, *A9*, 1–27.
(63) Jaacks, V. *Die Makromolekulare Chemie* **1972**, *161*, 161–172.
(64) Sevink, G.; Zvelindovsky, A.; Fraaije, J.; Huinink, H. *J. Chem. Phys.* **2001**, *115*, 8226–8230.
(65) Radzinski, S. C.; Foster, J. C.; Chapleski, R. C.; Troya, D.; Matson, J. B. *J. Am. Chem. Soc.* **2016**, *138*, 6998–7004.
(66) Singh, N.; Tureau, M. S.; Epps, T. H. *Soft Matter* **2009**, *5*, 4757–4762.
(67) Lin, T.-P.; Chang, A. B.; Chen, H.-Y.; Liberman-Martin, A. L.; Bates, C. M.; Voegtle, M. J.; Bauer, C. A.; Grubbs, R. H. *J. Am. Chem. Soc.* **2017**, *139*, 3896–3903.
(68) Dettmer, C. M.; Gray, M. K.; Torkelson, J. M.; Nguyen, S. T. *Macromolecules* **2004**, *37*, 5504–5512.
(69) Matyjaszewski, K.; Ziegler, M. J.; Arehart, S. V.; Greszta, D.; Pakula, T. *J. Phys. Org. Chem.* **2000**, *13*, 775–786.
(70) Sun, X.; Luo, Y.; Wang, R.; Li, B. G.; Zhu, S. *AIChE J.* **2008**, *54*, 1073–1087.
(71) Wang, R.; Luo, Y.; Li, B.-G.; Zhu, S. *AIChE J.* **2007**, *53*, 174–186.
(72) Radzinski, S. C.; Foster, J. C.; Scannelli, S. J.; Weaver, J. R.; Arrington, K. J.; Matson, J. B. *ACS Macro Lett.* **2017**, *6*, 1175–1179.
(73) Grubbs, R. H.; Khosravi, E. *Handbook of Metathesis: Polymer Synthesis*; Wiley, 2015.
(74) Slugovc, C.; Demel, S.; Riegler, S.; Hobisch, J.; Stelzer, F. *Macromol. Rapid Commun.* **2004**, *25*, 475–480.
(75) Xia, Y.; Kornfield, J. A.; Grubbs, R. H. *Macromolecules* **2009**, *42*, 3761–3766.
(76) Miyake, G. M.; Weitekamp, R. A.; Piunova, V. A.; Grubbs, R. H. *J. Am. Chem. Soc.* **2012**, *134*, 14249–14254.
(77) Radzinski, S. C.; Foster, J. C.; Matson, J. B. *Polym. Chem.* **2015**, *6*, 5643–5652.
(78) Wolfe, P. S.; Wagener, K. B. *Macromolecules* **1999**, *32*, 7961–7967.

(79) Rule, J. D.; Moore, J. S. *Macromolecules* **2002**, *35*, 7878–7882.
(80) Pollino, J. M.; Stubbs, L. P.; Weck, M. *Macromolecules* **2003**, *36*, 2230–2234.
(81) Seehof, N.; Grutke, S.; Risse, W. *Macromolecules* **1993**, *26*, 695–700.
(82) Liu, P.; Taylor, B. L. H.; Garcia-Lopez, J.; Houk, K. N.: Computational Studies of Ruthenium-Catalyzed Olefin Metathesis. In *Handbook of Metathesis*; Wiley-VCH Verlag GmbH & Co. KGaA, 2015; pp 199–252.
(83) Sanford, M. S.; Love, J. A.; Grubbs, R. H. *J. Am. Chem. Soc.* **2001**, *123*, 6543–6554.
(84) Adlhart, C.; Chen, P. *J. Am. Chem. Soc.* **2004**, *126*, 3496–3510.
(85) Vyboishchikov, S. F.; Bühl, M.; Thiel, W. *Chem. Eur. J.* **2002**, *8*, 3962–3975.
(86) Walsh, D. J.; Lau, S. H.; Hyatt, M. G.; Guironnet, D. *J. Am. Chem. Soc.* **2017**, *139*, 13644–13647.
(87) See Appendix A for the full derivation. We could not exclude the possibility that cycloaddition is the rate-limiting step, which would result in a more complicated rate expression.
(88) Further discussion of the ROMP mechanism can be found in Appendix A. We note that, at present, we cannot conclusively rule out an dissociate/associative pathway.
(89) Fürstner, A.; Thiel, O. R.; Lehmann, C. W. *Organometallics* **2002**, *21*, 331–335.
(90) Benitez, D.; Tkatchouk, E.; Goddard, W. A. *Organometallics* **2009**, *28*, 2643–2645.
(91) In-depth DFT investigation of the ROMP mechanism, including calculation of transition-state structures and identification of the rate-limiting step, will be the subject of future work.
(92) In order to account for pyridine binding, it is critical to use the same $[\mathbf{G3}]_0$ concentration in both homo- and copolymerization reactions. .
(93) Odian, G. *Principles of Polymerization*; 4th ed.; Wiley-Interscience: Hoboken, New Jersey, 2004.
(94) Meijs, G. F.; Rizzardo, E. *J. Macromol. Sci., Polym. Rev.* **1990**, *30*, 305–377.